1

2

3   Peer review status:

4   This is a non-peer-reviewed preprint submission to EarthArXiv

6

7

Smoothing Earth's surface: the complexity of soil texture class transitions

*Trevan Flynn[*1], Zahra Rasaei[2], Rosana Kostecki[3,4]*

[*1]Department of Agronomy, University of Forte Hare, Alice 5700 South Africa

[2]Department of Soil Science, University of Tehran, Karaj 77871 Iran

[3]Soil Consultoria Socioambiental, R. Prof. Joaquim de Matos Barreto, 88-Lima Azevedo, Londrina 86015 Brasil

[4]Department of Geography, State University of Londrina, Londrina 86055 Brasil

[*]Corresponding author email: trevanflynn@gmail.com
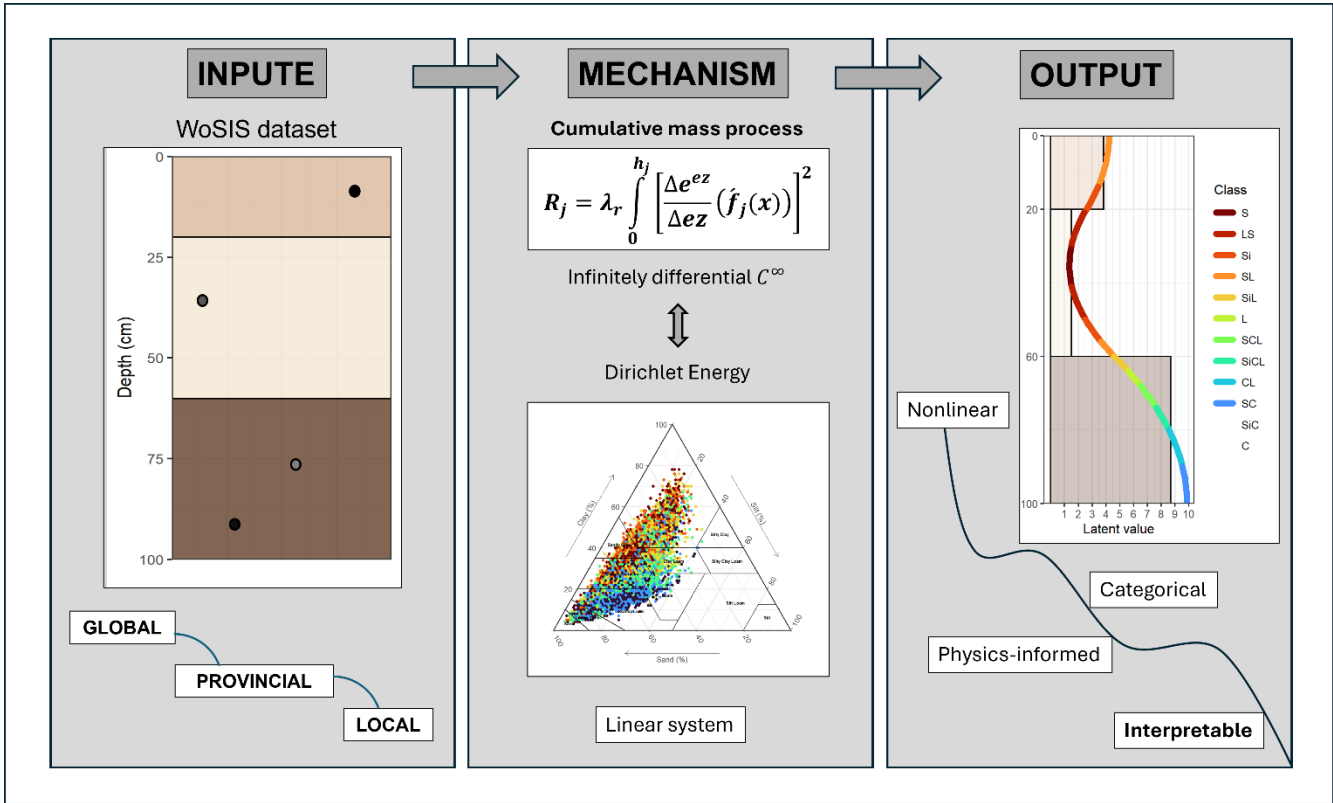
Abstract

Soil depth functions are essential for analysing, modeling, understanding and visualising soil profiles. While robust methods existed for continuous properties, soil texture is typically reported as discrete classes, and no established approach exists to interpolate soil categorical information with depth. Here, we introduced phySplines, a physics-informed, analytically solvable spline for interpolating soil categorical information. Soil texture classes were mapped to a latent numerical space and continuously interpolated by minimising the depth-weighted Dirichlet energy via the exact analytic integral of Euler's cumulative mass process, which encoded depth-dependent resistance and enforces non-parametric physically consistent smoothness. PhySplines achieved kappa values of 0.96, 0.94 and 0.96 at global, provincial and local scales, respectively. By embedding pedological theory within a fully continuous and interpolation framework, the function avoided over representation of dominant classes, captured previously unmodelled transitional states, mitigated the drift effect and generalised across missing layers. PhySplines maintained mass and energy continuity (infinitely differentiable C^{∞}) without over-constraining the solution, allowing for greater flexibility for future work into numerical classification and the quantification of soil thermodynamical multifunctionality. Ultimately, minimising potential energy and maintaining the mass contuninity, phySplines transformed complex soil profiles into dynamic, interpretable narratives, allowing users to "see" between horizons.

Keywords: Exact analytic integral; Depth function; Dirichlet Energy; Infinite Differentiability; Physics-informed

1 Introduction

Interpolation of properties with depth is a common practice across many scientific disciplines (Ma et al., 2026; Odom and Doctor, 2023; Probst et al., 2018; Rogozovsky et al., 2025; Zhao et al., 2025) and has become standard in soil analysis (Amundson et al., 2025; Benbi and Toor, 2026; Pei et al., 2025; Souza et al., 2023). Depth functions expand datasets by enabling harmonisation with other datasets (Cheng et al., 2024), improve understanding of soil profile physical (Zhang et al., 2023) and biochemical dynamics (Leewis et al., 2022) and support downstream applications in hydrology, ecology and environmental management (Ruiz et al., 2025). By providing representations that are mathematically robust yet easy to conceptualise and visualise, depth functions help facilitate communication with scientists, policymakers and communities.

Several approaches exist for representing soil properties with depth, including exponential decay (Kempen et al., 2011; Wiese et al., 2016), polynomials (Colwell, 1970; Russell and Moore, 1968), cubic splines (Flynn et al., 2022b), equal-area splines (ea-splines) (Bishop et al., 1999; Malone et al., 2009; Ponce-Hernandez et al., 1986) and grid-based ea-splines (Flynn et al., 2024). Unlike standard smoothing splines, ea-splines are formulated such that the integral of the spline equals the observed horizon mean, ensuring mass preservation with each horizon (Bishop et al., 1999; Ponce-Hernandez et al., 1986). Despite the benefits of continuous depth functions, limited soil profile observations may over-constrain them, leading to unrealistic values and increased criticism (Kienast-Brown et al., 2021).

Nevertheless, soil depth functions have rarely accommodated categorical data such as soil texture classes, which carry critical information for farmers, educators and land managers. The historical absence of robust methods for interpolating categorical data arises from the misconception that discrete soil classes do not exhibit boundary or transitional behavior (Burrough et al., 1997; Henderson et al., 2025) and partly from the inherent complexity of categorical mathematics (Basu and Isik, 2020; Yanofsky, 2015). Furthermore, traditional taxonomic dissemination tools are rarely designed for numerical modeling

65 (Zhang and Goodchild, 2002), creating bottlenecks that lead to information loss, computational

66 inefficiency and a disconnect between soil taxonomy and the quantitative requirements of environmental

67 models (Bortolus, 2008; Hillebrand et al., 2018; Isaac, 2004; Weiskopf et al., 2022).

68 The aim of this study was to develop phySplines, a physics-informed, analytically solvable spline for

69 interpolating categorical soil information to standardised depths across global, provincial and local

70 scales. Specifically, we sought to: (i) develop fully continuous, differentiable and mass-preserving

71 categorical splines that maintain pedological realism across spatial supports; (ii) incorporate physics-

72 informed constraints into an analytically solvable formulation, providing insight into class behaviour

73 while remaining computationally scalable without over-constraining; and (iii) develop a deterministic

74 spline capable of predicting "unseen" categories and inferring transitional or boundary classes suggested

75 by depth gradients, even when such classes were not directly observed in the profile. These innovations

76 introduce pedological realism by enforcing continuous, process-based gradients and transitions,

77 effectively bridging taxonomic information with the rigorous requirements of numerical environmental

78 modeling.

2 Methods and materials

2.1 Soil observations

81 To evaluate whether phySplines can be applied globally, across different spatial supports and for various

82 purposes, the spline was tested at three spatial scales. Data was obtained from the World Soil Information

83 Systems (WoSIS) dataset (ISRIC, 2021), which provides nearly global coverage. The global scale

84 encompassed most of the soil forming factors as well as soil functions that contribute to society and the

85 environment. Observations were included for analysis if they had United States Department of

86 Agriculture (USDA) soil texture classes assigned or had clay, silt and sand fractions summing to 100%

87 and the soil depth was ≤200 cm. A depth limit of 200 cm was applied because most international and

national soil classification systems, including the World Reference Base (WRB) and USDA Soil
Taxonomy, do not define diagnostic criteria beyond this depth. After filtering, a total of 101,568 soil
observations were retained for global analysis with or without missing horizons.

The WoSIS dataset included 6,791 observations (0.008 samples km^{-2}) at the provincial scale across New
South Wales (NSW), Australia (Figure 1), covering approximately 801,150 km² (center ≈147°1′E to
32°9′S). Elevation ranges from sea level to >2,000 m in the southeastern highlands. The geology is unique
with distinct sedimentary basins, with widespread sodic soil formed during episodes of landscape uplift
(Blewett, 2012). Climate and vegetation are highly variable across the province (Australian Bureau Of
Meteorology, 2019) with both winter and summer cropping systems represented (McDougall et al., 2002;
NSW Department of Primary Industries, 2020). Major urban centres are concentrated along the coast,
whereas inland areas are predominantly rural and agriculturally oriented (Smith and Robert B.
Thompson, 2019). The province was selected because it is among the most extensively studied regions
in quantitative pedology (e.g., the Hunter Valley), nearly all available profiles met the study criteria
(<200 cm depth and particle-size fractions summing to 100%) and the province encompasses a broad
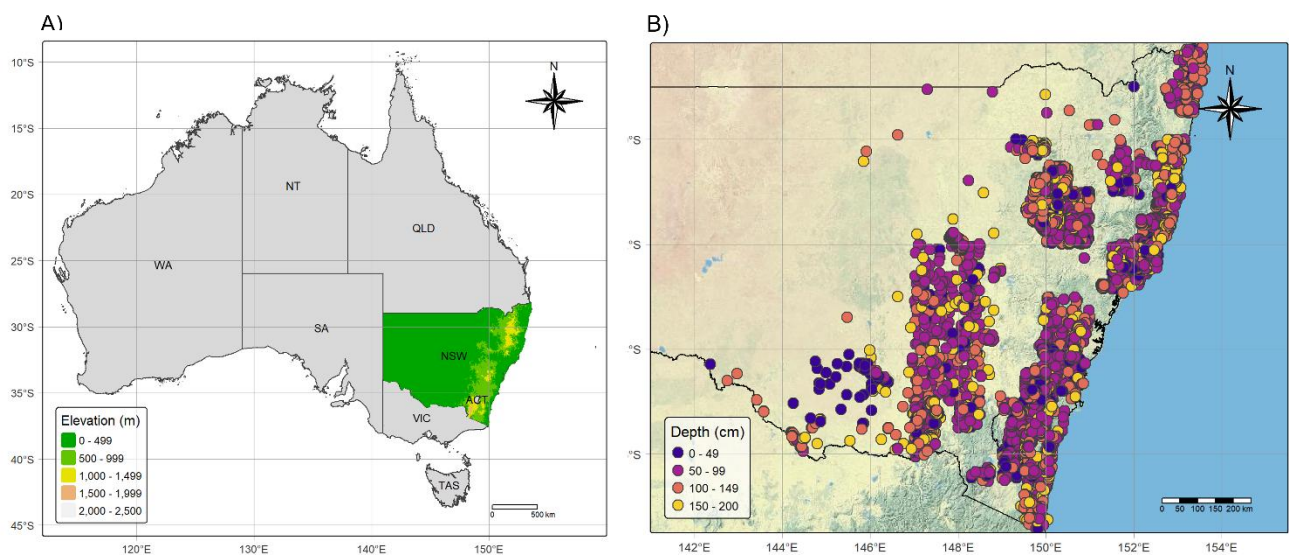range of environmental conditions relevant to pedogenesis.

Figure 1: The elevation of New South Wales (NSW) within Australia (A) and the soil observations with depth of NSW (B).

105 A region in southern Malawi (center ≈34°41′42″E, 15°26′42″S) was selected to evaluate phySplines at

106 the local scale due to the relatively high number of WoSIS soil observations (0.05 samples km^{-2}) within

107 a 1,191 km² area (Figure 2). Located northwest of Blantyre in the Neno District, there were 65 profiles

108 within and around a valley to the Lisungwe River, which drains to the Shire River, the primary outlet of

109 Lake Malawi. The elevation ranges from 256 to 1,635 m, corresponding to strong gradients in mean

110 annual temperature and precipitation (Fick and Hijmans, 2017). The region has a subtropical Udic soil

111 moisture regime and is dominated by smallholder agriculture, including tobacco, cotton, maize, soybean

112 and groundnut production (Araya et al., 2023). This site was selected because it provides sufficient profile

113 density to evaluate local-scale model behaviour and represents an environmentally sensitive landscape

114 relevant to soil–water and land-use management.
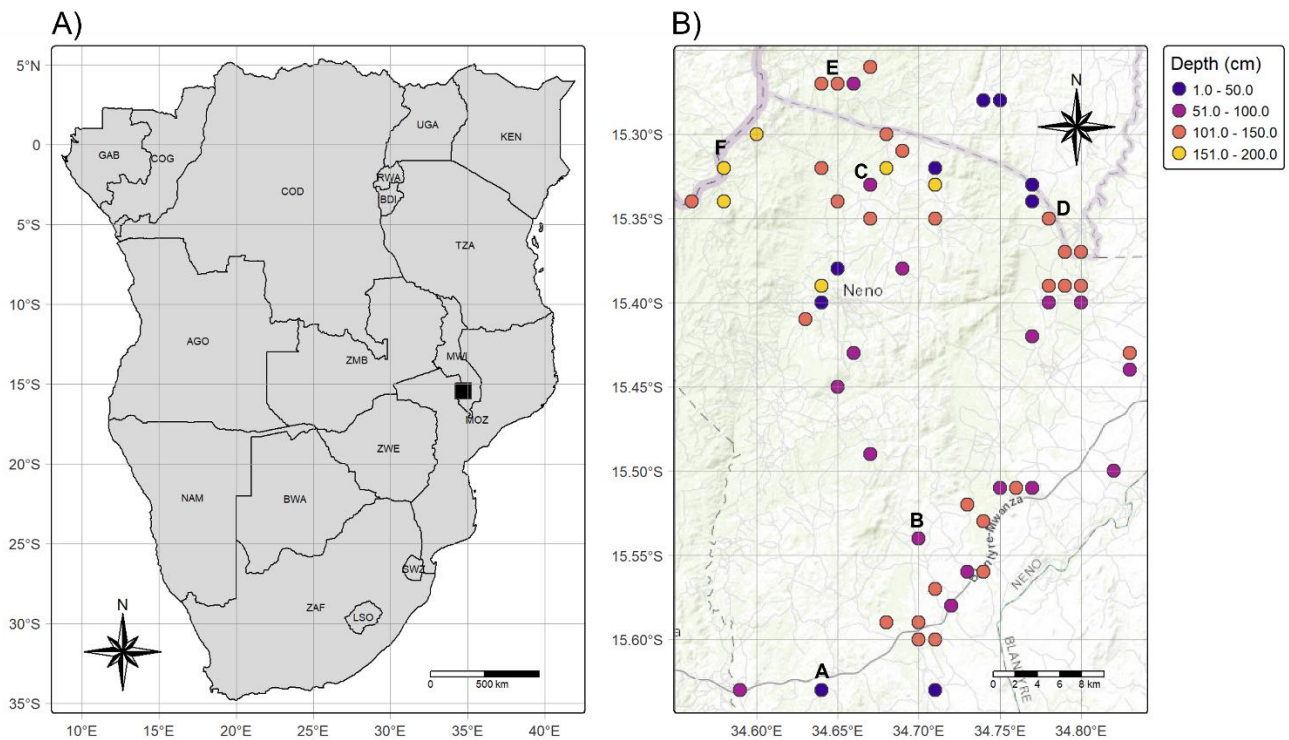
115

116 *Figure 2: Neno District (not to scale), Malawi within southern Africa (A) and the soil samples with depth within Neno District (B).*

117 Cross-scale validation was used to explicitly test the sensitivity of phySpline to observation density and

118 spatial heterogeneity. The global dataset spans highly variable soil environments with uneven sampling

densities, the NSW dataset represents a spatially biased setting with moderate observational support, and the Neno dataset reflects a dense but spatially constrained context. Consistent performance across these scales indicates that phySpline does not depend on scale-specific tuning or regional calibration, but instead derives stability from its physically constrained formulation.

For all scales, USDA soil texture classes comprised 12 categories, derived from clay, silt, and sand fractions on a texture triangle. The natural ordinal rank, from sand (1) to clay (1), was used for the physical process representing particle mass and surface area from the smallest to largest; the data was treated as unranked ordinal. Table 1 summarises the class symbols, names, latent value and the number of observations at the global, provincial and local scales.

Table 1: The United States Department of Agriculture (USDA) soil texture class symbol, name, latent value (Order) and the number of observations (n) for the global, provincial and local scales.

Class	Name	Order	Global (n)	Provincial (n)	Local (n)
S	Sand	1	28,390	824	3
LS	Loamy sand	2	28,511	1,400	50
Si	Silt	3	1,983	3	0
SL	Sandy loam	4	77,663	3,869	60
SiL	Silty loam	5	70,733	83	0
L	Loam	6	60,196	943	1
SCL	Sandy clay loam	7	35,856	4,024	56
SiCL	Silty clay loam	8	40,116	47	0
CL	Clay loam	9	35,977	1102	0
SC	Sandy clay	10	10,394	1,184	30
SiC	Silty clay	11	22,543	57	0
C	Clay	12	67,364	9,044	12

2.2   PhySpline theory

PhySplines are an energy-minimising function fitted through an exact integral function derived from classical mechanics. Along with the conservation of mass, the spline is based on potential energy, where the curve adjusts to maintain minimal energy through the cumulative mass of the soil column and boundary conditions with the surface, lithosphere and hydrosphere. In this case, we imposed a mathematical steady state by enforcing a zero flux and a geogenic steady state for the top and bottom horizons, respectively. Therefore, along with mass conservation, we enforce mass and energy continuity in a fully continuous, non-parametric function and move away from geometric midpoints toward the exact integral of the minimised energy.

2.2.1   Fundamental concept

To enable the use of categorical soil data, discrete soil texture classes were first mapped onto an ordered latent numerical axis by class symbols with order (Table 1). This ordinal transformation preserves the natural progression of texture from coarse to fine, allowing interpolation in continuous space while retaining categorical interpretability. Although soil texture triangles are conventionally defined by sand, silt and clay, the latent mapping flattened this multi-dimensional space into a one-dimensional sequence, with sand and clay as the endmembers. This simplification converts the complex multi-dimensional problem into a standard depth function, facilitating spline interpolation and process-based interpretation. This approach assumes that soil texture classes can be treated as ordinal data.

Each spline segment self-regularises, stiffening naturally with cumulative horizon mass according to an exponential process Euler's (e) cumulative mass process, effectively following a steady-state definite integral that limits unrealistic slopes. Latent values were then mapped to the nearest soil texture classes to produce harmonised, physically consistent profiles. Profile harmonisation was achieved by integrating the fitted latent values to the GlobalSoilMap standard depth intervals (0–5, 5–15, 15–30, 30–60, 60–100

154 and 100–200 cm). The harmonised dataset, source code, and the rafikisol R package (Flynn, 2023) are

155 available at www.github.com/rafikisol/rafikisol.

156 Key components of the phySpline formulation include:

157 • Continuous data fidelity: Observations contribute through a fully continuous loss function,

158 integrating across horizon thicknesses rather than relying on geometric midpoints.

159 • Definite integral: The spline was coefficients were estimated using the exact integral for the

160 entire profile, being infinite differentiable C^{∞}.

161 • Boundary conditions: The constraint matrix anchored the slope at the top and bottom, ensuring

162 the profile naturally returned to vertical at the boundaries.

163 • Physics-informed regularisation: The splines curve is dependent on the cumulative mass above

164 in a continuous manner from the Euler's cumulative mass process.

165 • Explicit matrix formulation: The design matrix A, regularisation matrix R and Jacobian

166 constraint matrix G are fully specified, enabling direct and transparent control over constraint

167 enforcement.

168 • Inter-horizon continuity: Continuity of both values (C^0) and first derivatives (C^1) are enforced

169 across horizon boundaries via a null-space projection of G, ensuring physically informed

170 constraints are satisfied exactly.

171 • Latent class preservation: Continuous latent values are mapped back to discrete soil texture

172 classes, maintaining interpretability while enabling continuous interpolation.

173 These central concepts of the phySpline go along with the paradigm shift in depth functions as we move

174 away functions that produce unrealist estimates. However, instead of using the point depth approach like

175 the USDA digital soil mapping focus team (Kienast-Brown et al., 2021); we decided to make sure the

176 spline was pedologically realistic, not over-constrained and obeyed physical laws.

2.2.2 Potential energy of soil

In phySplines, the soil profile is represented as a one-dimensional scalar field evolving within a potential-energy framework, where profile smoothness corresponds to the energetic cost of deformation. Since potential energy is defined through spatial gradients, this formulation aligns with pedological theory, in which soil profiles result from gravity-driven transport, diffusion and kinetically limited processes acting over depth and time (Hillel, 1998). This framework is not limited to pedology but is applicable across scientific disciplines, where potential energy provide the thermodynamic basis of soil multifunctionality and the capacity of soils to deliver ecosystem services (Kleidon, 2010). Therefore, this is not a random physics-informed theory, but one that is pedologically relevant and connects across disciplines, enhancing communication.

Within this framework, the soil profile is modeled as a scalar field $f(z)$ embedded in a heterogeneous medium with a depth-dependent resistance function $D(z)$. Under steady-state conditions, the profile minimises a weighted Dirichlet energy and satisfies the Euler–Lagrange equation:

$$\frac{d}{dz}\left(D(z)\frac{df(dz)}{dz}\right) = 0$$

with corresponding potential energy functional:

$$E[f] = \frac{1}{2}\int_{o}^{H} D(z)\left(\frac{df}{dz}\right)^2 dz$$

Here, $D(z)$ represents the local energetic resistance to slope change, reflecting mechanical and structural constraints of deeper soil layers due to compaction, overburden, clay illuviation and reduced biological mixing. This formulation naturally permits greater flexibility near the surface while progressively constraining curvature at depth, producing smooth and physically consistent profiles.

197   To model the monotonic increase in resistance while retaining analytical tractability, $D(z)$ is expressed

198   as an exponential function:

199
$$D(z) = D_o e^{kz}$$

200   which arises from the assumption that resistance increases proportionally to its current magnitude. The

201   exponential form of the resistance function arises naturally as the solution to a first-order growth process,

202   where the rate of change in soil stiffness is proportional to its current magnitude. The parameter k

203   represents the attenuation coefficient of pedological influence, while z defines the latent taxonomic

204   intensity, providing a coordinate system where physical stability is linked directly to the soil's

205   developmental state. The inclusion of Euler's number e ensures that this increase in resistance with depth

206   is both continuous and scale-independent.

207   ### 2.2.3   Physics-informed spline

208   The phySpline theory is expressed directly through the equations used in implementation, ensuring that

209   the mathematical formulation and computational realization are identical. The phySpline for each horizon

210   was expressed as a piecewise quadratic function:

211
$$f_j(x) = \alpha_j + b_j(x - u_j) + \gamma_j(x - u_j)^2,$$

212   where α_j is the value at the top of horizon j, b_j is the slope at the top of the horizon, γ_j controls the

213   curvature of the function within the horizon, and u_j is the top depth of horizon j. The curvature term γ_j

214   governs the redistribution of slope with depth, allowing internal deformation while maintaining

215   continuity at horizon boundaries. To estimate the coefficients $\beta = (\alpha_j, b_j, \gamma_j)$, data fidelity, regularisation

216   (roughness control), and inter-horizon continuity must be jointly enforced.

217   The data fidelity loss function was formulated as the continuous integral over each horizon to preserve

218   the exact mean, numerical stability and class structure.

219
$$L(A) = \frac{1}{2}||y - A\beta||_2^2 = \frac{1}{n}\sum_{j=1}^{n}\left(\int_0^{h_j} f_j(x)dx - y_j\right)^2$$

220   where h_j is the thickness of horizon j and the integral measures the squared difference between the spline-

221   interpolated values $f_j(x)$ and the observed values y_j.

222   For the regularization term, pedological theory governs the conceptual model, physics governs the

223   horizons, with smoothness arising from the minimisation of potential energy within each horizon. Spline

224   smoothness was governed by a depth-weighted Dirichlet energy defined through the exact analytic

225   integral of a global Euler cumulative mass process. Rather than treating regularisation as a numerical

226   penalty or imposing boundary conditions, the energetic cost of deformation was integrated over each

227   horizon, allowing smoothness and curvature to emerge naturally from the profile itself. For horizon j,

228   the energy minimised was

229
$$R_j = \lambda_r \int_0^{h_j} \left[\frac{\Delta e^{ez_j}}{\Delta ez_j}[\acute{f}_j(x)]\right]^2 dx,$$

230   where $f_j(x)$ is the piecewise polynomial representing the profile, h_j is the horizon thickness, ez is the

231   global normalised depth $z \in [0,1]$. The exponential term represents a depth-dependent stiffness,

232   reflecting increasing mechanical and structural resistance with depth, while the difference-quotient

233   formulation evaluated resistance as a physically meaningful process that is infinitely differentiable C^∞.

234   Cumulative mass resistance was defined globally and integrated over finite horizons creating boundary

235   behaviour that emerged naturally from the exact analytic integral. Therefore, the top horizon collapses

236   to a point evaluation at $z = 0$, the basal horizon to $z = 1$ and interior horizons are governed by the

237   integral means of the stiffness process. Smoothing was thus confined strictly to the soil domain,

238   preventing boundary drift, align with the constraint matrix, while maintaining physically consistent

239   continuity and curvature.

240   Data continuity between horizons represents a physical requirement for mass conservation and structural

241   integrity. These constraints were encoded in a Jacobian matrix G, enforcing both C^0 and C^1 continuity

242   across horizons:

243
$$\|G\beta\|_2^2 = G\beta = 0,$$

244
$$f_j(h_j) - f_{j+1}(0) = 0 \ (C^0 \ continuity),$$

245
$$f_j'(h_j) - f_{j+1}'(0) = 0 \ (C^1 \ continuity),$$

246

247   Boundary slope constraints were applied at the top and bottom of the profile to anchor the spline, maintain

248   numerical stability and maintain a mathematically steady state. Together with R, the boundary conditions

249   create a zero flux and geogenic boundary for the top and bottom horizon, respectively. To enforce all

250   constraints exactly while retaining a linear system, the coefficient vector was projected into the null-

251   space of G:

252
$$\beta = N\gamma,$$

253   where N spans the null-space of G. Within this projected space, the horizon-level roughness penalties

254   R_j are combined into a global, profile-aware roughness matrix, representing the total energetic cost of

255   profile deformation:

256
$$R = N^T \left(\sum_j R_j \right) N$$

257   This transformation converts the constrained energy minimisation problem into an unconstrained system

258   in γ, ensuring exact horizon continuity while preserving the physical interpretability of the roughness

259   penalty. In this way, continuity constraints were satisfied exactly, the roughness penalty remained

260   physically interpretable and the solution efficiently balances fidelity to observed data with minimisation

261   of the profile's potential energy. The objective function is then formulated as:

262    $$\mathcal{L}(\gamma) = \frac{1}{2} \parallel y - AN\gamma \parallel_2^2 \; + \; \lambda_r \, \gamma^\top N^\top RN\gamma.$$

263   Solving for γ yields the reduced-order ordinary least squares solution, and the full coefficient vector is

264   recovered as $\beta = N\gamma$. This approach guarantees exact horizon continuity while balancing smoothness

265   against fidelity to the observed data. Crucially, the roughness term R arises from the definite integral of

266   the Euler cumulative mass process, embedding global, depth-dependent stiffness directly into the loss

267   function. The governing system is linear and reflects steady-state physics, and the phySpline solution is

268   obtained analytically through energy minimisation, producing an optimal, closed-form set of coefficients

269   that captures physically consistent curvature and emergent boundary behaviour across the profile.

270   Once a spline's coefficients were estimated, the integral for any standardised depth interval can be

271   directly calculated or continuous curves can be interpolated and fitted values $f_i(x)$ are mapped to soil

272   classes by nearest latent class (Table 1):

273    $$c_i = \arg \min_i \mid f_i(x) - l_i \mid,$$

274   where l_i are latent class values and c_i is the interpolated soil texture class at location (e.g., interval, cm,

275   mm, etc) i. This approach provides a simple, computationally efficient and intuitive classification of the

276   full vertical soil profile.

277   2.2.4   Generalisation and missing horizons

278   Many studies have discussed the idea of adding pseudo horizons to anchor boundary conditions at the

279   top and bottom of the profile or as an anchor when there are discrete boundaries (Bishop et al., 1999;

280   Malone et al., 2009; Odgers et al., 2012; Ponce-Hernandez et al., 1986). Notably, many authors noted

challenges with abrupt changes or the "drift" effect common in quadratic splines. To handle missing or unsampled depths, pseudo horizons were introduced to stabilise phySpline coefficients. Missing depths were initially imputed using the median of adjacent horizons, providing placeholders for coefficient estimation. Once spline coefficients were computed, imputed horizons were removed from the system and treated as extrapolated regions. However, no pseudo-horizon was added to address drift, as the energy-minimising solution naturally curves back to a vertical slope.

2.2.5 Spatial prediction

At the provincial scale, harmonised soil texture classes were predicted across the 90 m Soil and Landscape Grids of Australia (ASRIS, 2024; CSIRO, 2024) to provide spatial representations and visualise vertical variation along transects. Predictions were generated for six standard depth intervals, using 18 covariates representing clay, silt, and sand fractions within each depth interval (Malone and Searle, 2022; Viscarra Rossel et al., 2014). Gradient tree boosting was used for spatial prediction due to its ability to capture complex environmental relationships without over-predicting dominant soil classes (Flynn et al., 2019). Gradient tree boosting is an eager learner that precomputes a model during training (from soil profiles), making prediction across grids computationally efficient (Hastie et al., 2009; Kuhn and Johnson, 2013). For each depth interval, all grid layers were used as covariates, i.e., the independent variables consisted of texture fractions from 0–200 cm. Mathematically, the predicted soil texture class $\hat{C}_k$ for class k is:

$$\hat{C}_k \approx \sum_{m=1}^{M} L_m H_m(clay_k, silt_k, sand_k),$$

where M is the total number of trees, L_m is the learning rate, and H_m is the m-th tree in the sequence, trained to iteratively improve predictions from the previous tree.

2.3 Validation and plausibility

2.3.1 Reference splines

Two reference splines (controls) were implemented to illustrate the methodological progression from standard continuous interpolation to the phySpline framework. This progression is intended as a demonstration of specific enhancements, rather than a formal comparative study, highlighting the steps required to resolve categorical transitions while retaining the simplicity and statistical robustness of the ea-spline framework.

The first reference spline, C-EAS was a canonical ea-spline adapted to classify where data fidelity was the geometric mean, and the regularization term was the first derivative penalty. Therefore, continuity is implicitly implied through the geometry of the fidelity term

$$\mathcal{L}_{C-EAS}(\beta) = \frac{1}{2}||A\beta - y||_2^2 + \lambda_r \beta R\beta.$$

The C-SoftG reference spline was a non-canonical intermediate spline where there is a trade off between data fidelity, smoothness and continuity. The terms are the same as the ea-spline and continuity matrix is the same as the phySplines,

$$\mathcal{L}_{C-SoftG}(\beta) = \frac{1}{2}||A\beta - y||_2^2 + \lambda_r \beta R\beta + ||G\beta||_2^2.$$

2.3.2 Statistical validation

PhySpline performance was evaluated across multiple scales using overall accuracy, Cohen's kappa (Cohen, 1960) and the latent value Root Mean Squared Error (RMSE) for λ_r values of 0.5, 0.25, 0.10, 0.05 and 0.01. These values were selected following Bishop et al. (1999) and other studies on ea-splines such as Malone et al. (2009) and . This approach ensured that scale-specific performance reflected robustness to data availability, rather than simply spatial extent, providing a controlled stress test. To

select an appropriate λ_r for the control and subsequent analyses, a sensitivity analysis was performed using L-curve curvature maximisation at the global scale. The "elbow" of the curve, corresponding to the peak of the second derivative of the LOESS-smoothed RMSE profile, identifies the transition between under- and over-fitting.

For individual soil texture classes, recall (producer's accuracy), precision (user's accuracy), bias and F1 scores were calculated to evaluate the ability of phySplines to classify both dominant and underrepresented classes. Harmonised uncertainties were quantified as the absolute distance between predicted values and the nearest latent class, providing a measure of confidence across both occupancy and transitional classes. These uncertainties were subsequently scaled to a range of 0–1.

Spatial predictions were evaluated in a similar manner, using an 80/20 split for training and evaluation. Overall accuracy was computed to assess predictive performance. While the primary focus of this study is phySpline performance, evaluation of spatial predictions ensured that mapped representations of soil texture are meaningful, reliable for visualisation purposes and were comparable to other studies.

2.3.3   Physical plausibility

To evaluate the behaviour and physical consistency of the phySpline solutions, we computed a set of diagnostics for profile:

- Kink (C^1 Continuity): The absolute difference between the bottom slope of one horizon and the top slope of the next, capturing derivative discontinuities at horizon boundaries.
- Energy (Roughness): The quadratic form $\beta^T R_s \beta$ for each horizon, representing the contribution of the horizon to the spline's regularisation term. Higher energy indicates significant internal "stretching" to accommodate the data.

345   • Mass jump (Mass): The ratio of horizon thickness h_j to the total profile depth H_{tot}, representing

346   the volumetric leverage of the layer.

347   • Mismatch (C^0 Continuity): The absolute difference between the predicted value at the base of

348   horizon j and the intercept of horizon $j + 1$, quantifying value discontinuities across horizons.

349 These diagnostics provide complementary measures of smoothness, physical realism, and horizon-level

350 behavior, allowing both global and horizon-specific assessment of spline performance.

351 To summarise spline physical plausibility, we combined the diagnostics into a composite metric. Let K_i

352 denote the interfacial kink, E_i the internal energy, M_j the horizon mass jump, and $M_{m,i}$ the boundary

353 mismatch. Weighted root-mean-square (RMS) values were computed for kink and energy as:

$$354 \qquad K_{RMS} = \sqrt{\frac{\sum_{i=1}^{n}(K_i\, M_j)^2}{\sum_{i=1}^{n} M_j}}$$

$$356 \qquad E_{RMS} = \sqrt{\frac{\sum_{i=1}^{n}(E_i\, M_j)^2}{\sum_{i=1}^{n} M_j}}.$$

355

357 The RMS of mismatch is calculated as:

$$359 \qquad \text{Mismatch}_{RMS} = \sqrt{\frac{1}{n}\sum_{i=1}^{n} M_{m,i}^2}.$$

358

360   Weighting kink and energy by M_j ensures that structural integrity of the primary soil mass is prioritized

361   over localized noise in thin horizons. The Integrated Process Score (ISP) metric is then defined as the

362   average of these three RMS values:

363
$$\text{ISP} = \frac{\text{Kink}_{\text{RMS}} + \text{Energy}_{\text{RMS}} + \text{Mismatch}_{\text{RMS}}}{3}.$$

364   To assess whether predicted classes preserve information from observed classes, Mutual Information

365   (MI) was calculated:

366
$$I(X;Y) = \sum_{x \in X} \sum_{y \in Y} p(x,y) \log \left(\frac{p(x,y)}{p(x)p(y)} \right),$$

367   where X is the observed soil texture class, Y the predicted class, $p(x,y)$ the joint probability of $X = x$

368   and $Y = y$, and $p(x)$, $p(y)$ the marginal probabilities. MI was normalized to the range $[0,1]$ by dividing

369   by the maximum MI within each group. This captures transitions across the two-dimensional structure

370   of Depth $\times$ Classes [1–12], which would be missed in a one-dimensional, depth-only analysis (e.g.,

371   continuous depth).

372   This formulation favors economical, process-clamped solutions, where latent profiles transition smoothly

373   with depth. It serves as a structural validation metric, ensuring that spline-derived numeric values

374   produce a physically consistent soil column before categorical assignment. In other words, MI quantifies

375   how much information the predictions preserve about observed classes while maintaining realistic, depth-

376   continuous transitions.

377 3 Results

378 3.1   Comparisons

379   The results of the phySpline at each scale followed the same general pattern (Table 2). As λ_r decreased,

380   phySpline performance increased, with higher accuracy, kappa values and lower latent-space errors.

381   These patterns, however, were most pronounced at the global scale with an 80% reduction in λ_r (from

382   0.50 to 0.10) resulting in a 44% increase in kappa, from 0.76 to 0.95. A further 90% reduction in λ_r (from

383   0.10 to 0.01) was associated with a 4% increase in kappa, from 0.95 to 0.99. The corresponding RMSE

384   decreased from 0.37 at $\lambda_r = 0.50$ to 0.13 at $\lambda_r = 0.10$ (65% decrease in errors), and further to 0.02 at

385    $\lambda_r = 0.01$ (85% decrease in errors). Therefore, there is a strong relationship between λ_r, accuracy, kappa

386   and RMSE. Thus, the elbow method on the global data revealed a $\lambda_r = 0.10$ was the slope steepened

387   past this point indicating potential overfitting.

388   *Table 2: The scale, lambda (λ_r), overall accuracy, kappa and the latent RMSE.*

Scale	λ_r	Accuracy (%)	Kappa	RMSE
Global	0.50	70	0.66	0.37
	0.25	89	0.89	0.21
	0.10	97	0.96	0.11
	0.05	100	1.00	0.01
	0.01	100	0.99	0.02
Provincial	0.50	77	0.72	0.37
	0.25	87	0.83	0.25
	0.10	96	0.94	0.13
	0.05	100	0.99	0.02
	0.01	100	1.00	0.02
Local	0.50	78	0.72	0.34
	0.25	92	0.89	0.23
	0.10	97	0.96	0.12
	0.05	100	1.00	0.01
	0.01	100	1.00	0.02

389

390   At the provincial scale, kappa increased from 0.66 at $\lambda_r = 0.50$ to 0.94 at $\lambda_r = 0.10$, reaching 1.00 at

391    $\lambda_r = 0.05$. Over the same range, RMSE decreased from 0.37 to 0.13 and then to 0.02. over the same

392   range. At the local scale, kappa increased from 0.72 at $\lambda_r = 0.50$ to 0.96 at $\lambda_r = 0.10$, and to 1.00 at

393    $\lambda_r = 0.05$. The RMSE decreased from 0.34 to 0.12 and to 0.02 across the same range.

394   The C-SoftG control achieved statistical performance comparable to phySpline across all scales (Table

395   3). At the global scale, accuracy reached 97%, with a kappa of 0.96 and an RMSE of 0.14. At the

396   provincial scale, accuracy, kappa, and RMSE were 95%, 0.90, and 0.14, respectively. At the local scale,

397   C-SoftG achieved an accuracy of 93%, a kappa of 0.90, and an RMSE of 0.19. The C-EAS had nearly

398   perfect statistical performance at all scales.

399   *Table 3: The reference splinel accuracy-based measures showing the scale, λ_r, overall accuracy, kappa, RMSE of the residuals*

400   *and the uncertainties of the harmonised depth intervals.*

Spline	Scale	λ_r	Accuracy	Kappa	RMSE
C-SoftG	Global	0.10	97	0.96	0.14
	Provincial	0.10	95	0.93	0.14
	Local	0.10	93	0.90	0.19
C-EAS	Global	0.10	100	1.00	<0.01
	Provincial	0.10	100	1.00	<0.01
	Local	0.10	100	1.00	<0.01

401

402   At all scales, the IPS is comparatively lower with 0.15, 0.31 and 0.15 for the global, provincial and local

403   scales respectively. However, all indices were best performing at the global scale with the lowest IPS

404   and highest MI (1.00). The provincial scale, similar to the statistical analysis, had moderate performance

405   with a slightly higher MI of 0.85 and the local scale had a MI of 0.88. It should be noted that these results

406   are not comparable across models as the curves are fitted in different ways and the energy indicates a

407 different measure. However, the C-SoftG had the same trend and C-EAS techniqually doesn't have these

408 measures but were gathered anyways to see if they were like the statistics and produce misleading results.

409 *Table 4: Process based parameters showing mean energy, kink, MassJump, mismatch, Integrated Process Score (IPS) and*

410 *Mutual Information (MI).*

Spline	Scale	Kink	Energy	MassJump	Mismatch	IPS	MI
phySpline	Global	0.00	0.14	0.20	0.00	0.15	1.00
	Provincial	0.00	0.58	0.29	0.00	0.31	0.85
	Local	0.00	0.49	0.30	0.00	0.15	0.88
C-SoftG	Global	0.01	0.26	0.20	0.41	0.43	0.94
	Provincial	0.00	0.60	0.29	4.00	3.14	0.85
	Local	0.00	0.61	0.30	1.85	1.69	0.85
C-EAS	Global	0.00	0.00	0.20	17.7	9.60	1.00
	Provincial	0.00	0.00	0.29	23.0	11.5	1.00
	Local	0.00	0.00	0.30	16.6	7.60	1.00

411 .

412 Figure 3A–C presents example soil profiles illustrating continuity, mismatch, kink behavior and class–

413 process alignment for the three models. The phySpline (Figure 3A) produced a smooth latent profile that

414 crossed horizon boundaries exactly at observed class transitions while also resolving intermediate

415 transitional classes along the latent scale. In contrast, the C-SoftG model correctly interpolated each

416 horizon to its observed class but showed erratic curvature and limited representation of transitional

417 classes between horizons (Figure 3B). The C-EAS model achieved perfect classification accuracy;

418 however, the fitted curve and resulting classes strictly followed horizon boundaries allowing no transitory

419 behaviour, yielding no meaningful internal structure beyond exact mathematical conformity (Figure 3C).
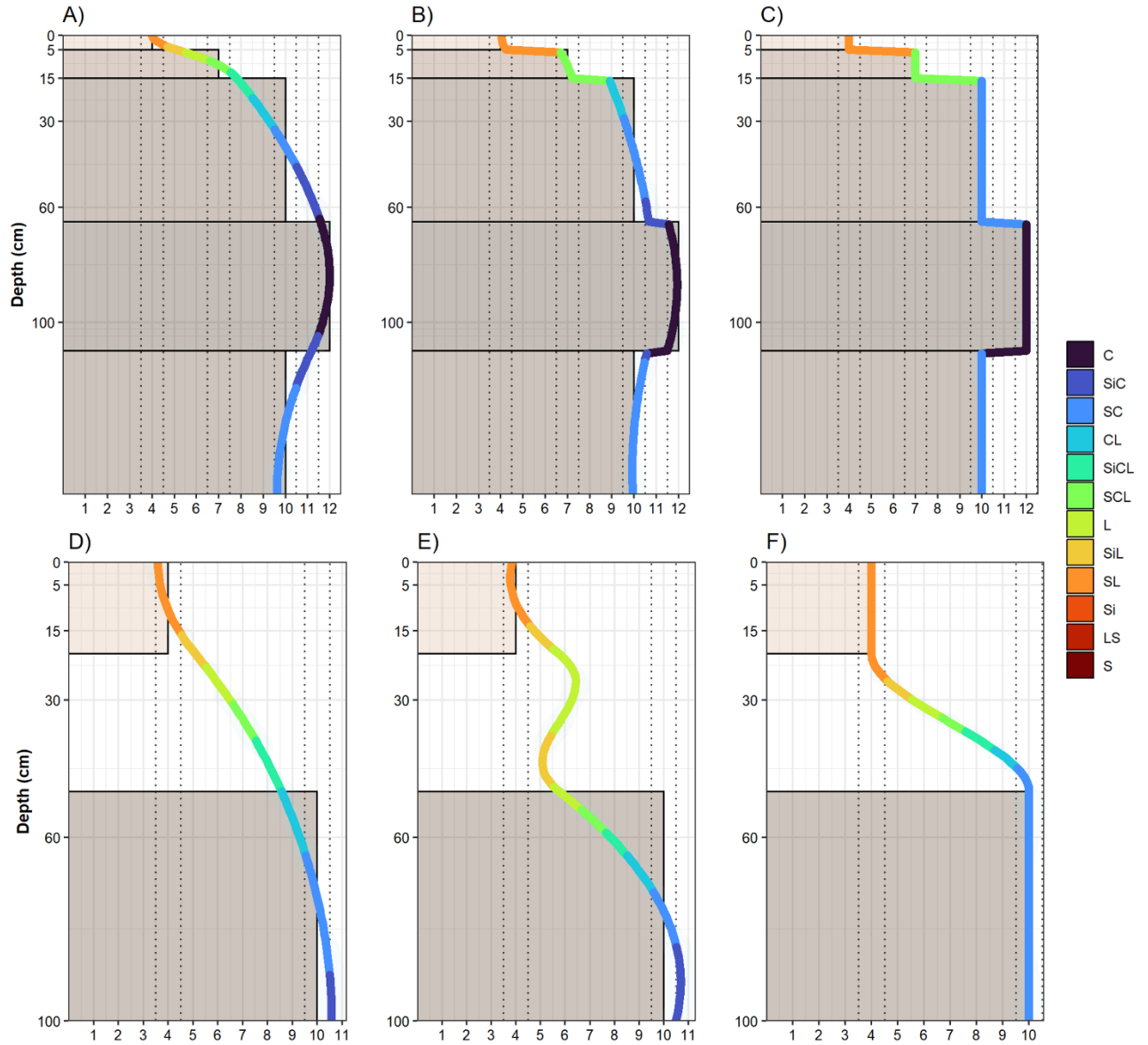
Figure 3E–G show extrapolated profiles for the phySpline, C-SoftG (without a ghost horizon) and C-EAS (without a ghost horizon). The phySpline maintained smooth, physically coherent transitions under extrapolation (Figure 3E), whereas the absence of a ghost horizon in C-SoftG resulted in increased instability near profile boundaries (Figure 3F). The C-SoftG model was evaluated without a ghost horizon to illustrate the effects of extrapolation in the absence of artificial anchoring, whereas ghost horizons

24

428 were used for all other C-SoftG analyses. Notably, C-EAS captured transitional classes more effectively

429 when horizons were absent, but this behavior was suppressed when horizons were present (Figure 3G).

430 ## 3.2 Global scale

431 The global model took 8 min and 40.09 seconds to run 101,568 profiles through the linear ODE equation.

432 Despite moderate class imbalance (observed occurrence ranging from 16.2% for SL to 0.41% for Si), all

433 classes achieved F1 scores ≥ 0.80 except Si (F1 = 0.58; Table 4). Absolute occupancy bias remained

434 within ± 1.00 percentage points for all classes except C (− 1.20), with the C class (14.0% observed

435 occupancy) slightly underpredicted. The Si class exhibited high recall (0.90) but low precision (0.43),

436 reflecting increased false-positive assignment for this rare texture class, which was slightly over

437 predicted. All other soil texture classes had unbiased predictions according to a 1.00% threshold.

438 *Table 5: The observed prevalence and predicted prevalence, prediction bias, precision, recall and F1 scores at the global scale.*

Class	Observed (%)	Predicted (%)	Bias	Precision	Recall	F1
C	14.0	12.8	-1.20	1.00	0.91	0.95
SiC	4.70	5.28	0.58	0.78	0.87	0.82
SC	2.17	2.70	0.54	0.74	0.92	0.82
CL	7.50	7.25	-0.25	0.95	0.92	0.93
SiCL	8.36	8.56	0.19	0.92	0.94	0.93
SCL	7.47	7.71	0.24	0.91	0.93	0.92
L	12.6	13.1	0.58	0.91	0.95	0.93
SiL	14.7	14.6	-0.11	0.95	0.93	0.94
SL	16.2	15.5	-0.64	0.99	0.95	0.97
Si	0.41	0.86	0.45	0.43	0.90	0.58
LS	5.94	5.91	-0.04	0.95	0.94	0.94
S	5.91	5.59	-0.33	0.99	0.94	0.97

439

440 Class occupancy of harmonised depth intervals revealed systematic vertical trends in global soil texture

441 distributions (Figure 4). Clay content increased with depth, rising from 9.40% at 5–15 cm to 16.60% at

442 60–100 cm (76% increase). However, stronger depth-related increases were observed for SiC and SC.

443 The SiC class increased from 2.73% at 0–5 cm to 5.81% at 30–60 cm (113% increase), followed by a

slight decline to 5.09% at 100–200 cm. SC increased from 1.79% at 0–5 cm to 4.75% at 60–100 cm

(166% increase). Both SiC and SC exhibited higher associated uncertainty, with mean uncertainty values

of 0.27 and 0.39, respectively. Silty loam decreased from 19.8% at 5–15 cm to 10.9% at 60–100 cm (45%

change), while SL declined from 18.7% at 0–5 cm to 11.5% at 100–200 cm (38% change). These classes

exhibited comparatively low median uncertainty (0.15 for SiL and 0.14 for SL). In contrast, S showed

minimal depth dependence, with only a 31% change across the profile, decreasing to 23% occupancy at
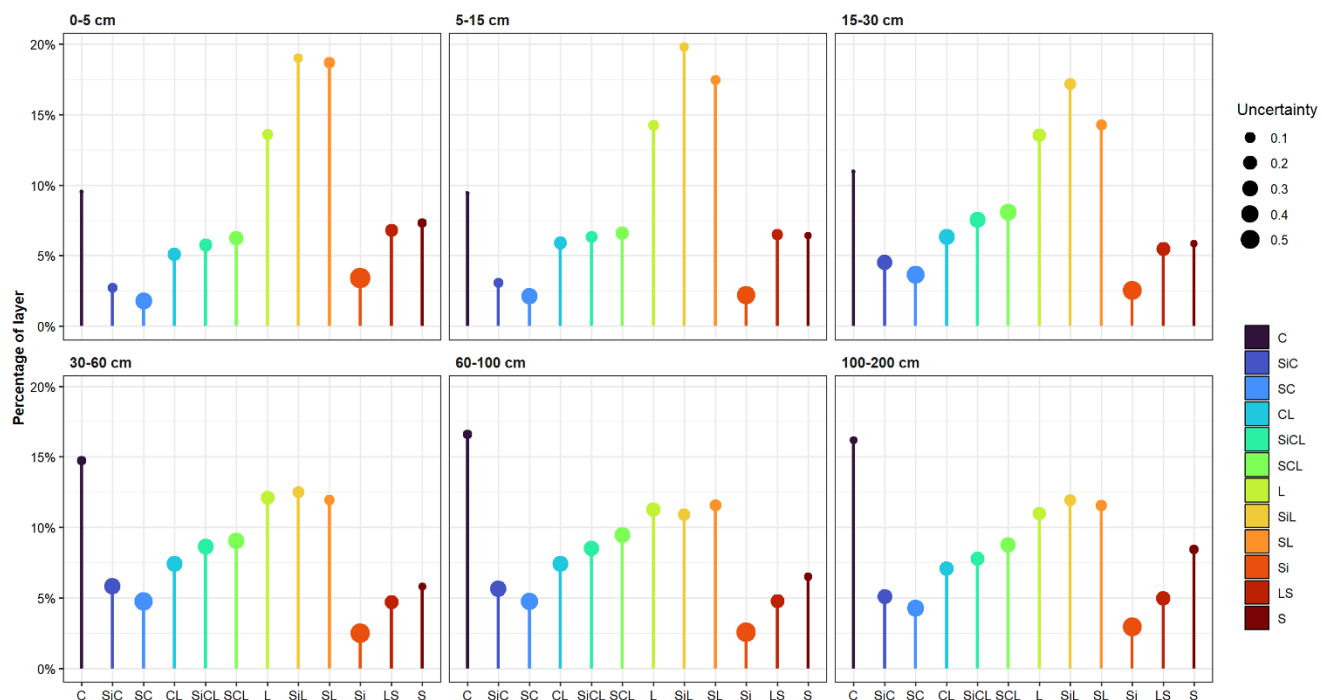
depth.

Figure 4: The percent proportion of each soil texture class for the GlobalSoilMap depth intervals with their uncertainties.

Depth-resolved structural diagnostics of the phySpline profiles revealed systematic variation across

the harmonised depth intervals (Table 6). The phySpline was computationally zero for kink and mismatch

was expected. For energy, it ranged from 0.314 at 100-200 cm to 0.493 at the 0-5 cm range when

corrected for depth width. This mirrors the IPS which also slowly declined with depth from 0.164 to

0.104, while MI was over 0.99 and remained independent of depth.

26

458 *Table 6: Process-based validation showing the root mean square of* Kink$_{rms}$, Energy$_{rms}$, IPS and MI

Spline	Intervals	Kink$_{rms}$	Energy$_{rms}$	Mismatch$_{rms}$	IPS	MI
PhySpline	0-5 cm	0.000	0.493	0.000	0.164	0.998
	5-15 cm	0.000	0.409	0.000	0.136	0.999
	15-30 cm	0.000	0.391	0.000	0.130	0.998
	30-60 cm	0.000	0.378	0.000	0.126	0.999
	60-100 cm	0.000	0.359	0.000	0.120	0.998
	100-200 cm	0.000	0.314	0.000	0.104	0.996
C-SoftG	0-5 cm	0.004	0.191	1.478	0.557	0.992
	5-15 cm	0.004	0.153	1.227	0.461	0.975
	15-30 cm	0.004	0.150	1.293	0.482	0.942
	30-60 cm	0.004	0.140	1.245	0.463	0.921
	60-100 cm	0.005	0.128	1.212	0.450	0.922
	100-200 cm	0.003	0.107	1.395	0.501	0.941
C-EAS	0-5 cm	0.000	0.000	31.79	10.69	1.00
	5-15 cm	0.000	0.000	29.49	9.829	1.00
	15-30 cm	0.000	0.000	31.58	10.53	1.00
	30-60 cm	0.000	0.000	31.22	10.40	1.00
	60-100 cm	0.000	0.000	32.33	10.78	1.00
	100-200 cm	0.000	0.000	33.62	11.21	1.00

459

460   The composite IPS, integrating kink, energy and mismatch, decreased with depth from 0.165 in the 0–

461 5 cm interval to 0.105 in the 100–200 cm layer, highlighting progressively lower structural penalties in

462 deeper horizons. These patterns were consistent across more than 1.5 million horizon-level observations,

with the number of profiles per interval ranging from 140,031 (0–5 cm) to 610,964 (30–60 cm). The C-SoftG Kink ranged from 0.00334 at 100–200 cm to 0.00415 at 0–5 cm. The Energy decreased from 0.191 at 0–5 cm to 0.107 at 100–200 cm, whereas Mismatch remained elevated (1.22–1.47), reflecting less precise horizon alignment than phySpline. The depth-resolved IPS ranged from 0.451 at 60–100 cm to 0.557 at 0–5 cm. Profile counts matched those of phySpline, enabling direct comparison.

The C-EAS profiles showed minimal interfacial discontinuities (Kink 1.13–2.79×10^{-16}) and negligible internal roughness (Energy $\sim 10^{-29}$), but exhibited very large boundary misalignments (Mismatch 29.5–33.6), resulting in correspondingly high IPS values (9.83–11.2). Depth trends were relatively stable across intervals, with shallow layers (0–5 cm) showing slightly lower IPS than deeper horizons. The MI scores with harmonised depths follow that of the whole profile with all C-EAS having the highest MI followed by phySplines and C-SoftG.

3.2   Provincial scale

This visualisation approach required spatial analysis from the phySplines prior to implementation at the provincial scale. The spatial classification accuracy was approximately 50% across depth intervals, with a maximum of 54%. Similar spatial accuracies, despite good depth-function performance and realistic class distributions, have been reported previously (Flynn et al., 2024, 2022a). In this case, the spatial results were sufficient to support further profile-level analysis. Two transects, indicated by black and blue circles in the 0–5 cm layer and the black and blue transects (length $\approx$ 60–70 km) of the predicted classes (Figure 5), were therefore selected for visualisation of phySpline behaviour.
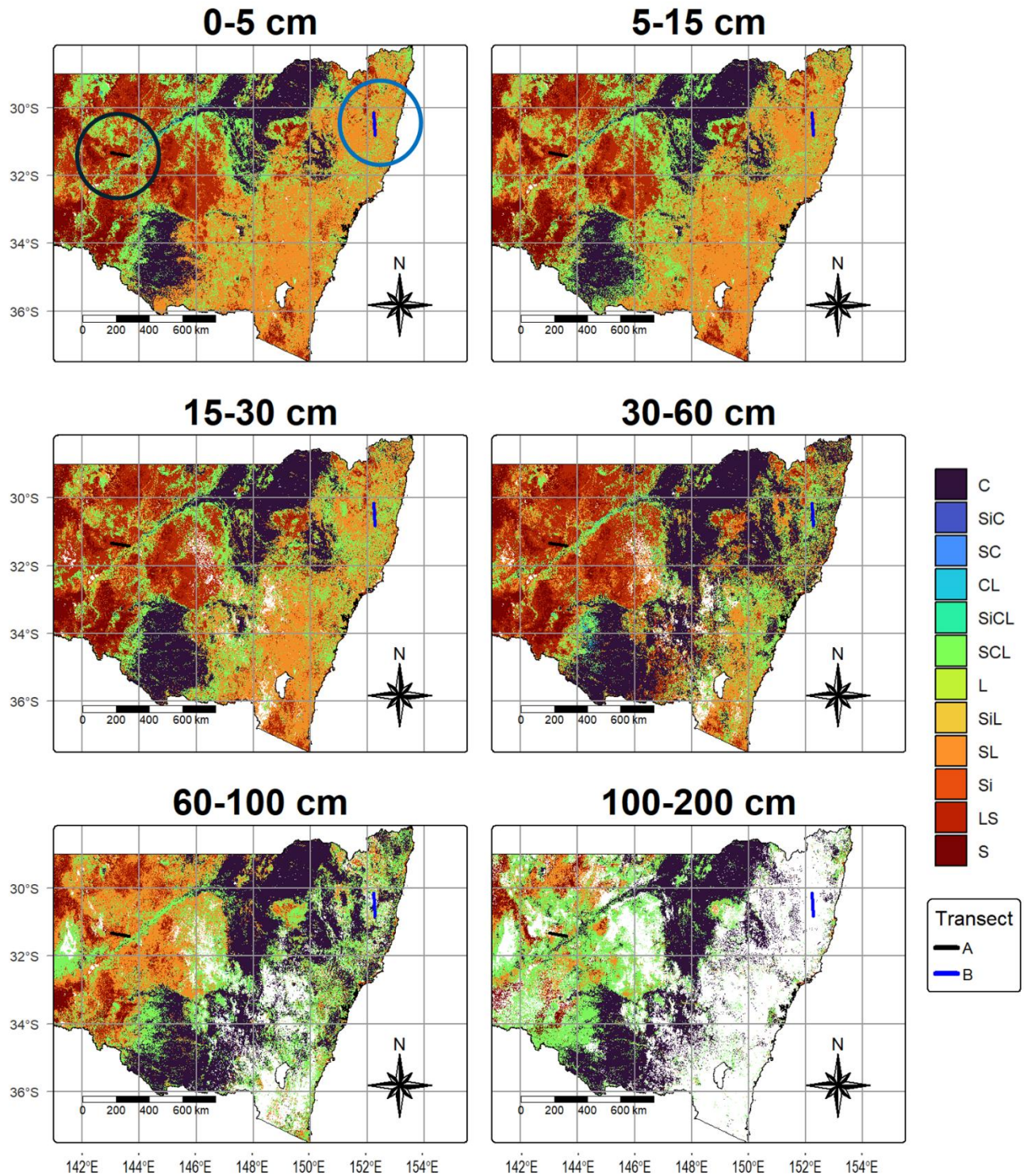
Figure 5: Predictions for New South Wales, Australia using phySpline harmonised texure classes as training data.

Both transects span approximately 60–70 km. Transect A is located in the semi-arid western region and

runs west to east, while transect B traverses the more topographically variable, subtropical eastern region

from north to south. Transect A captures a higher number of pixels, providing finer spatial detail, whereas
transect B covers a larger pixel area, resulting in a coarser but simplified visualisation. These transects
illustrate differences in spatial resolution and visual representation across contrasting landscapes.
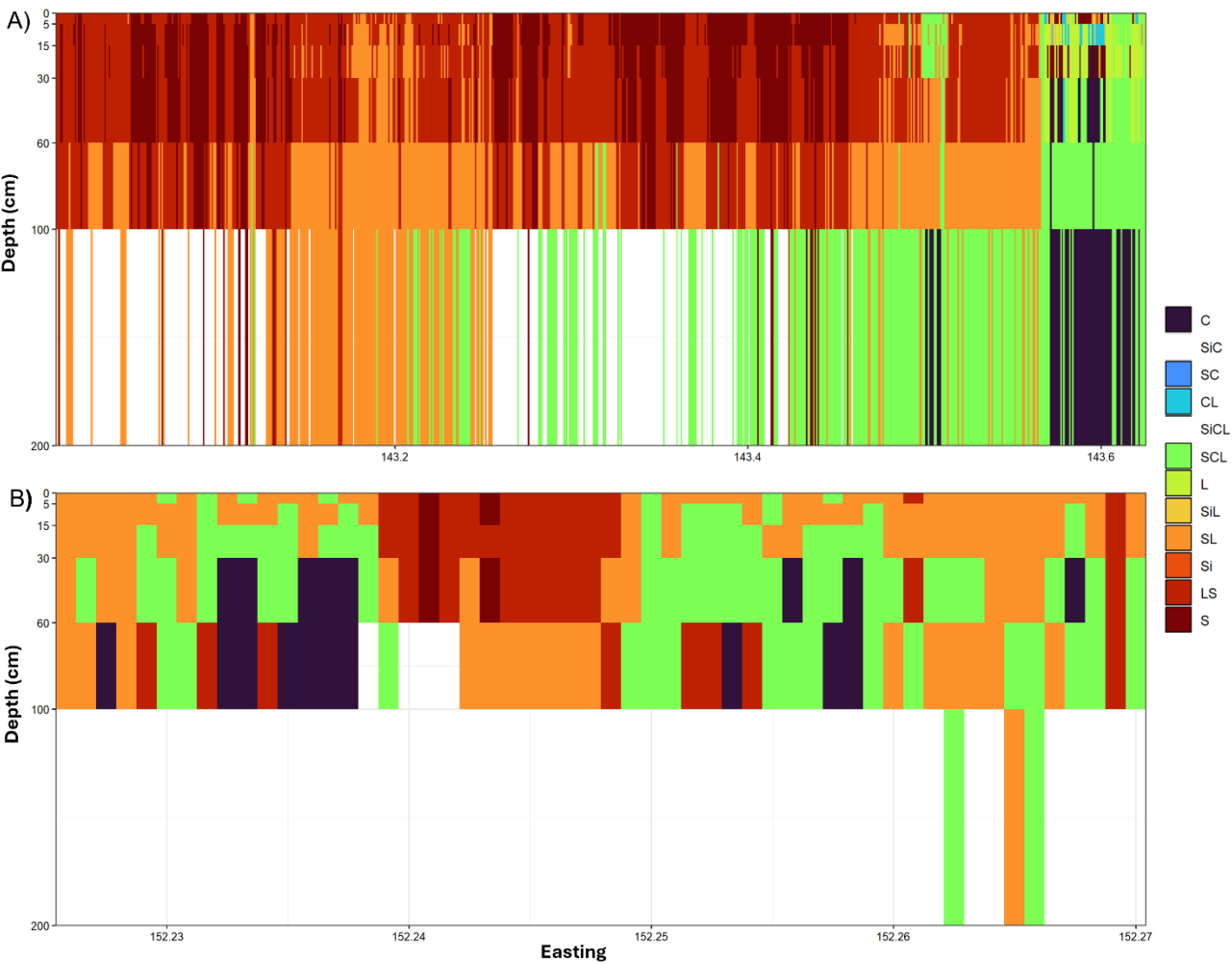
Figure 6: Cross sections used to display transects of the soil texture class (A) and each transect with depth intervals (B,C). The transects x-axis runs latitude or from west to east.

The provincial scale exhibited the greatest class imbalance (Table 7), with C occupying 40% of the
dataset, yet it was underpredicted by less than 1.00% and remained with balanced predictions. In contrast,
the spline overpredicted the SiC class, but only by 0.67% and misclassification decreased gradually away

from the dominant class in a systematic manner. Therefore, although the dataset was imbalanced, the

496 predictions remained balanced and like the global scale.

497 *Table 7: Confusion matrix for from phySplines interpolation on the WoSIS dataset in NSW, Australia.*

	C	SiC	SC	CL	SiCL	SCL	L	SiL	SL	Si	LS	S	Recall
C	8665	343	32	3	1	0	0	0	0	0	0	0	0.96
SiC	0	52	4	1	0	0	0	0	0	0	0	0	0.91
SC	0	7	1122	52	2	1	0	0	0	0	0	0	0.95
CL	0	0	16	1060	24	2	0	0	0	0	0	0	0.96
SiCL	0	0	0	0	44	3	0	0	0	0	0	0	0.94
SCL	0	0	1	14	161	3786	56	6	0	0	0	0	0.94
L	0	0	0	0	1	19	919	3	1	0	0	0	0.97
SiL	0	0	0	0	0	1	7	75	0	0	0	0	0.90
SL	0	0	0	0	0	4	5	145	3707	8	0	0	0.96
Si	0	0	0	0	0	0	0	0	0	3	0	0	1.00
LS	0	0	0	0	0	0	0	2	7	78	1313	0	0.94
S	0	0	0	0	0	0	0	0	2	5	24	793	0.96
Precision	1.00	0.13	0.95	0.94	0.19	0.99	0.93	0.32	0.99	0.03	0.98	1.00	0.96

498

499 The Si class, despite its low prevalence, exhibited an apparent 100% accuracy, while most other classes

500 achieved accuracies above 90%, except for SiC (86% accuracy). The high false positives can be seen in

501 all the low prevalence classes of SiC (13%), SiCL (19%), SiL (32%) and Si (3%) which had an original

502 prevalence of 0.25, 0.20, 0.37 and 0.01 in the dataset, respectively. Therefore, although the high accuracy

503 of each class, the precision and recall give insight into the transition classes.

504 Class-resolved structural diagnostics revealed systematic, method-specific differences in spline

505 performance (Figure 7). For phySpline, IPS values remained low across all classes (0.20–0.77), with

506 contributions dominated by internal energy rather than boundary discontinuities or boundary

507 mismatches. The lowest IPS was observed for coarse loams (CL = 0.20), whereas the highest occurred

508 in fine silty textures (Si = 0.77), reflecting slightly higher internal variation in these classes. C-SoftG

509 exhibited moderate energy penalties coupled with substantial boundary mismatches (IPS ≈ 3–4.7),

510 particularly in transitional textures such as SiL and SiC. In contrast, C-EAS displayed negligible Kink

511 and energy penalties, but extreme boundary misalignments (IPS ≈ 6–17) across all classes, highlighting

512 its perfect local fit at the expense of global structural fidelity.
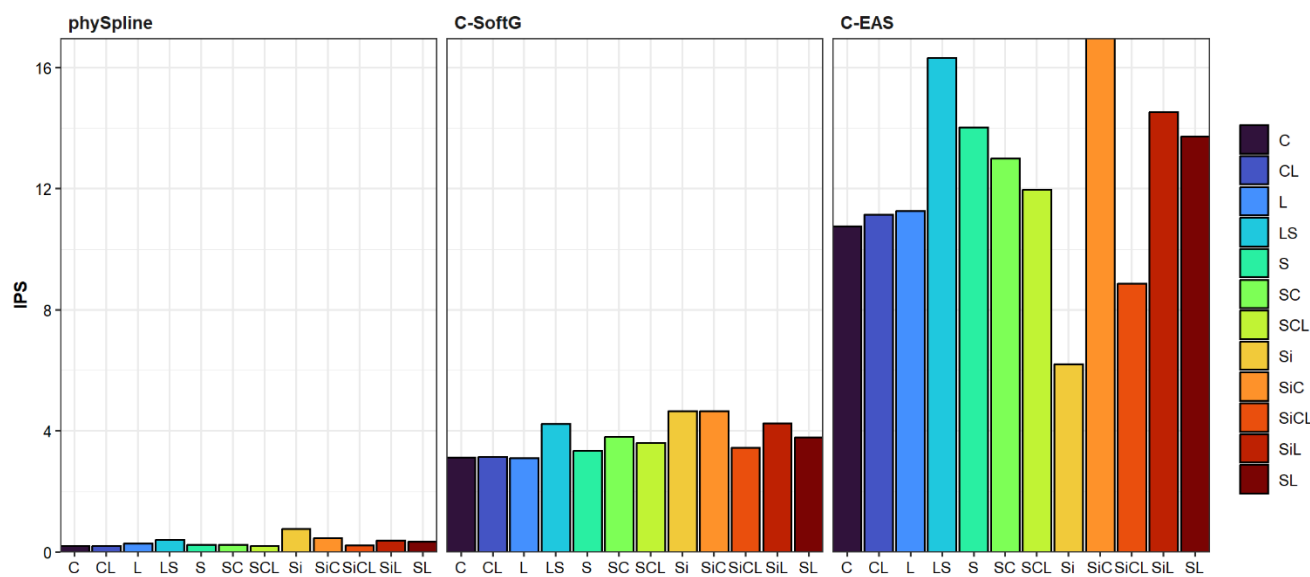
513

514 *Figure 7: The Integral Process Score (IPS) for the C-EAS, C-SoftG and the phySpline for and its correspondence to each class.*

515 ### 3.3   Local scale

516   The Neno District dataset included 65 soil profiles with evenly represented soil texture classes (Figure

517 8). The only comparison with the reference splines was if the splines were over constrained with 0.00,

518 0.00 and 68.9 for the phySpline, C-SoftG and C-EAS, respectively. From these, six profiles were selected

519 (Figure 2) for detailed analysis and overlaid with gridded environmental variables, including mean

520 annual precipitation (MAP), mean annual temperature (MAT), elevation, slope, aspect and landform

521 element (LFE). The selected profiles varied in depth, from shallow (Profile A, 35 cm) to deep (Profile F,

180 cm), and exhibited diverse texture patterns, ranging from shallow, coarse-textured profiles (Profile B, LS-SL, 35 cm) to deep, very fine textured soil (Profile E, SC-C, 150 cm). All profiles had low IPS of 0.10, 0.06, 0.05, 0.20, 0.03 and 0.04 for A, B, C, D, E, F and G, respectively.
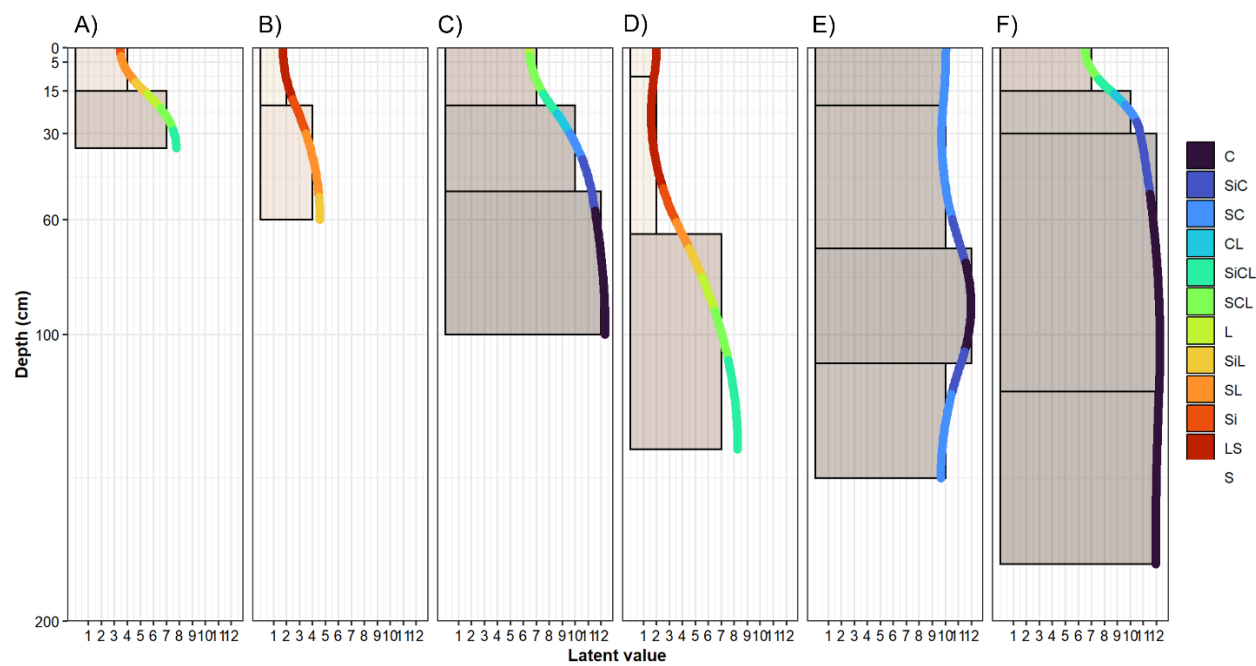

Figure 8: The selected profile's phySplines curve with their latent value on the y-axis to show how they correspond down the profile.

The selected profiles represented a broad spectrum of pedogenetic factors, requiring a model capable of adapting to diverse depth and texture patterns (Table 8). Environmental conditions across the site ranged from high-altitude, high-precipitation mountain slopes to low-relief, high-temperature depositional hollows. Profile F was located at 1,419 m elevation with high annual rainfall (96 mm) on a steep slope (15.1%), whereas Profile D was in a low-relief hollow (2.16% slope) with lower rainfall (76 mm) and higher mean annual temperatures (24 °C). Profiles A, B and C represent intermediate conditions on slopes and spurs, with slopes ranging from 4.47 to 9.60 degrees reflecting the steep topography of the Neno region.

Table 8: Environmental factors for each selected profile showing mean annual precipitation (MAP), mean annual temperature (MAT), elevation DEM, slope, aspect, landform element (LFE) and normalised mutual information per interpolated profile.

Profile	MAP (mm)	MAT (ºC)	DEM (m)	Slope (%)	Aspect	LFE	MI
A	80	24	521.0	4.47	203	Slope	0.63
B	73	25	358.0	4.49	93.5	Spur	0.63
C	97	22	951.0	9.60	297	Slope	1.00
D	76	24	442.0	2.16	145	Hallow	0.58
E	95	20	1,261	16.7	50.5	Spur	0.51
F	96	19	1,419	15.1	119	Spur	0.95

The harmonised uncertainty profiles (Figure 9) provide a standardised measure of model confidence across soil horizons. These profiles capture uncertainty associated with the discrete depth intervals used in the phySpline solution, reflecting stability across harmonised depth intervals (Table 8). Uncertainty values appear to be largely independent of the phySpline curves and environmental factors. Thin layers exhibited both high and low uncertainty (e.g., A = 0.95, D = 0.03), while subsoil horizons (60–100 cm) also showed variable uncertainty (D = 0.75, E = 0.17). Profiles in contrasting landscape settings, such as

545　　B in the Lisungwe valley with low rainfall and E in mountainous, steep terrain, displayed similar

546　　uncertainty patterns at 5–15 cm (B = 0.01, E = 0.04).
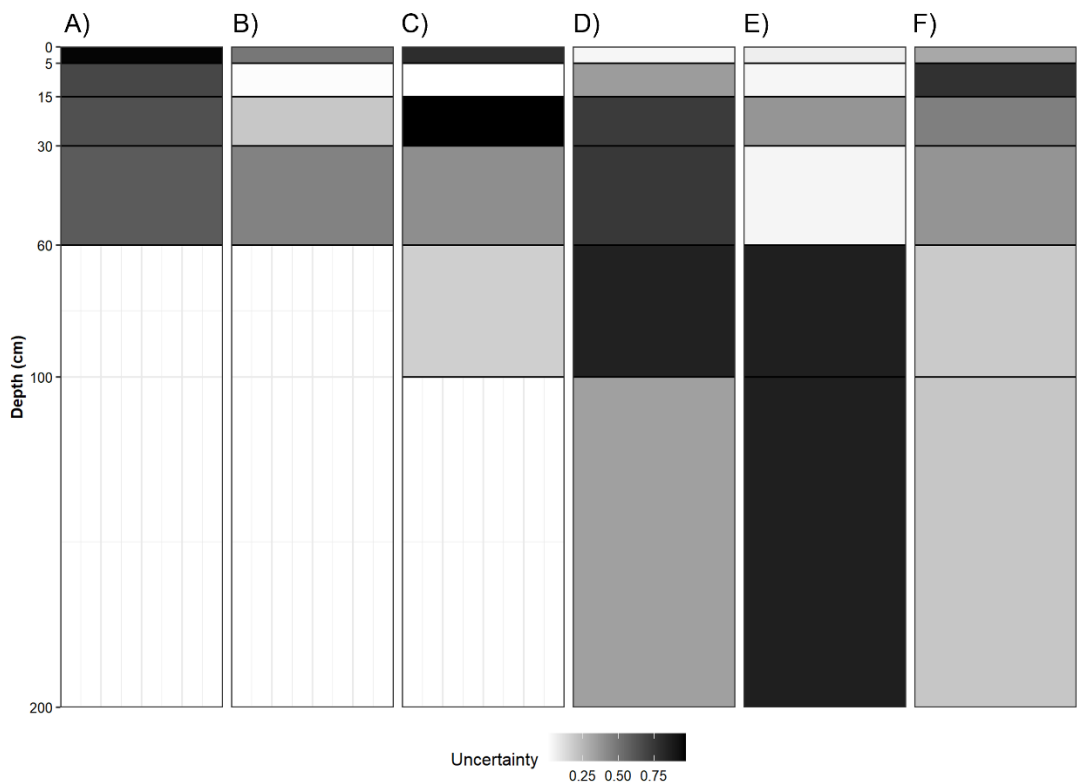
547

548　　*Figure 9: The uncertainties associated with the selected profiles shown for the harmonised soil depths.*

549　　Major classes with substantial observations, such as C, SC, SCL, SL, LS and S, were accurately

550　　predicted, showing recall values between 0.90 and 1.00. Some minor or sparsely represented classes

551　　(e.g., SiC, CL, SiCL, SiL, Si) had no observations in the test set, resulting in undefined recall and

552　　precision. Nevertheless, there were seven classes present in the dataset and 11 in the interpolated set. Yet

553　　misclassifications were minimal and mostly occurred between closely related classes, such as SC and

554　　SL, or SCL and L.

555

556

Table 9: Confusion matrix of the phySplines interpolation on the WoSIS dataset in the Neno District, Malawi.

	C	SiC	SC	CL	SiCL	SCL	L	SiL	SL	Si	LS	S	Recall
C	12	0	0	0	0	0	0	0	0	0	0	0	1.00
SiC	0	0	0	0	0	0	0	0	0	0	0	0	NA
SC	0	0	28	2	0	0	0	0	0	0	0	0	0.93
CL	0	0	0	0	0	0	0	0	0	0	0	0	NA
SiCL	0	0	0	0	0	0	0	0	0	0	0	0	NA
SCL	0	0	0	0	1	54	1	0	0	0	0	0	0.96
L	0	0	0	0	0	0	1	0	0	0	0	0	1.00
SiL	0	0	0	0	0	0	0	0	0	0	0	0	NA
SL	0	0	0	0	0	0	0	2	58	1	0	0	0.97
Si	0	0	0	0	0	0	0	0	0	0	0	0	NA
LS	0	0	0	0	0	0	0	0	0	1	49	0	0.98
S	0	0	0	0	0	0	0	0	0	0	0	3	100
Precision	1.00	0.00	1.00	0.00	NA	1.00	0.50	0.00	1.00	0.00	1.00	1.00	0.97

4 Discussion

Building on the foundation of previous work, we developed the phySpline: a categorical, physics-informed, and analytically solvable spline for interpolating soil classes with depth. The model is designed to capture pedological philosophy through gradient thresholds, where information is held in the form of potential energy within the soil profile, and resistance to change is governed by an Euler cumulative mass process. To illustrate its performance and novelty, we compared it against two reference spline: a modified equal-area spline capable of classification (C-EAS) and an intermediate spline incorporating a continuity matrix (C-SoftG). The splines were evaluated using the WoSIS dataset at global, provincial (NSW, Australia), and local (Neno District, Malawi) scales. Validation considered both statistical performance and physical realism to determine whether the observed spline behaviour reflected genuine pedological patterns or merely mathematical coincidences. This multi-scale evaluation highlights the ability of the phySpline to maintain process-based continuity, structural fidelity, and pedological interpretability across diverse soil environments.

4.2.1 Spline performance and lambda

Across all spatial supports, phySplines exhibited a consistent and interpretable relationship between the regularisation parameter λ_r, predictive accuracy, kappa and RMSE (Table 2). Decreasing λ_r systematically increased overall accuracy and agreement while reducing RMSE, demonstrating that λ_r functions as a physically meaningful process-based control rather than a purely statistical tuning parameter. At the global scale, an 80% reduction in λ_r (0.50 - 0.10) produced a disproportionate improvement in model performance (kappa $\approx$ 0.66 - 0.93; RMSE $\approx$ 0.37 - 0.13), whereas further reductions yielded diminishing returns. This clear inflection supported the use of the elbow criterion to identify $\lambda_r = 0.10$ as the optimal point that balanced fidelity and generalisation.

The phySplines framework demonstrated exceptional numerical stability, maintaining structural integrity even when λ_r was reduced to 1.0×10^{-5}. Unlike traditional splines, which typically exhibit erratic "hooking" or oscillatory behaviour at low smoothing levels, phySplines remained physically consistent. This stability is attributed to the Euler cumulative mass process, where depth-dependent resistance (e^{kz}) acts as an internal physical damper.

By prioritising the exact analytic integral of the mass reservoirs over pointwise midpoint estimates, the model achieved kappa values of 0.94–0.96 without over-constraining the solution. The high fidelity to horizon observations does not result in a "staircase" effect; instead, the minimisation of the weighted Dirichlet Energy ensures that transitions between texture classes are represented as continuous gradients. This allows for the capture of transitional states (the latent taxonomic shifts between horizons) that are often lost in discrete classification or over-smoothed continuous models.

4.2.2 Physics-informed, process-based and self-regularised

The intent of the reference functions was not for benchmarking but to contextualise the progression from purely statistical splines to a physics-informed, process-based formulation. While accuracy metrics alone

595   suggest broadly comparable performance at $\lambda_r < 0.10$, this can mask fundamental differences in

596   structural behaviour (Table 3). PhySplines uniquely enforced continuity through a null-space projection

597   and the integrals used, yielding exact slopes (zero kink, C^1), exact values (zero mismatch, C^0), horizon

598   boundaries space ($z \in [0, 1]$), and smooth internal curvature simultaneously. This contributed to low

599   internal potential energy and high mutual information, producing a physically realistic spline with strong

600   and independent class resolve. Even when horizons appeared visually discrete, maintaining mass

601   continuity when interpolating or harmonising to new depth intervals was critical, as it preserved the

602   integrity of pedogenic transitions and ensured that derived thresholds reflected the underlying, physically

603   coherent soil structure in unsampled locations (Table 4). The phySpline remained unconstrained for all

604   scales.

605   By contrast, the C-EAS achieved perfect local fits by construction but oversimplified profile structure

606   and suppressed transitional behaviour, resulting in extreme boundary mismatches at the profile scale

607   (high IPS and MI). This produced splines that were statistically enhanced but physically implausible,

608   effectively overfitting the data at the expense of continuity and was over-constrained for all scales.

609   Nevertheless, it reflects the philosophical view that soil classes are inherently discrete and may carry

610   limited physical meaning, a perspective of conceptual significance. The C-SoftG remained

611   unconstrained, with a moderate IPS and MI, allowed smoother transitions but sacrificed derivative

612   continuity and boundary alignment. PhySplines were the only approach to resolve these trade-offs

613   explicitly, embedding soil-process realism directly into the analytical solution rather than relying on post

614   hoc constraints.

615   Although MI was relatively high across all splines, Figure 3A demonstrates that phySplines maintained

616   continuity in both depth and latent space without disconnects between transitions. Visually, this indicates

617   that when harmonising soil texture classes, phySplines correctly integrate over the new depth interval.

618   Figure 3B and 3C illustrate latent value mismatches for C-SoftG and C-EAS, highlighting structural

619   divergence despite high numerical accuracy. Figure 3E shows the clear stability effect phySplines

620   pseudo-horizon had on the coefficients, while Figure 3F demonstrated the clear need to impute the

621   median. Unexpectedly, C-EAS transitions between classes without knowledge of a horizon, a behaviour

622   the deserves further investigation

623   These findings indicate that phySplines reconstruct vertically coherent soil profiles consistent with

624   pedogenic theory, reframing depth functions as minimising the potential energy of the soil profile through

625   the exact integral of the cumulative mass. By uniting visual fidelity, physical plausibility and categorical

626   integrity, phySplines provide a fully interpretable framework to see between horizons, capturing both

627   subtle and abrupt pedogenetic transitions in a continuous, process-informed manner.

628   ### 4.2.3   Global scale: process realism and depth-structured soil behaviour

629   Having established that phySplines respond to regularisation in a scale-independent and physically

630   interpretable manner, the global-scale results demonstrated how this behaviour translated into

631   pedologically realistic depth structure. At this extent, phySplines maintained stable class behaviour

632   despite moderate imbalance in class frequencies (Table 5). Dominant texture classes were not amplified,

633   while rare classes were retained as meaningful components of the latent process space rather than

634   suppressed or absorbed. Misclassifications occurred primarily among neighbouring texture classes,

635   reflecting transitional uncertainty rather than categorical failure. This behaviour is consistent with

636   pedological expectations, where soil texture transitions were gradual and classes represent discretised

637   interpretations of the underlying continuum.

638   Depth-resolved behaviour further supported this interpretation. A systematic vertical organisation of

639   texture classes emerged across class domain, with finer textures preferentially expressed at depth and

640   coarser or loamy textures concentrated near the surface (Figure 4). The C, SiC, and SC classes exhibited

641   signs of illuviation around 60 cm and remained stable through the remainder of the profile, whereas SiL

642   and SL followed the opposite trend. Nevertheless, these overall patterns aligned with established

643   pedological processes such as eluviation–illuviation, residual enrichment, and cumulative weathering

644   (Buol et al., 2011; Jenny, 1941). These trends were recovered without explicit depth stratification or

645   class-specific constraints. Mutual information remained high and independent of depth, exceeding 0.99

646   across all harmonised intervals, indicating strong class fidelity, while C-SoftG exhibited decreasing

647   values with depth, suggesting reduced structural coherence in deeper horizons.

648   Uncertainty was not associated with depth-related class behavior; it neither tracked class-specific depth

649   trends nor displayed an independent, quantifiable trend with depth. However, they were also independent

650   of number of observations, making it challenging to interpret and seemingly decoupled from the system.

651   However, these uncertainty estimates provide useful contextual information within the harmonised

652   dataset. For example, the Si class exhibited relatively more and consistent uncertainty at the global scale

653   than any other classes, or we can be 60% certain that the interpolations are Si from 15 – 60 cm. This is

654   also where SL and LS, the neighboring classes start to decline and were Si reaches its uncertainty plateau.

655   This structure arises from the physics-informed, energy-minimising formulation of phySpline (Table 6).

656   From top to bottom, energy gradually declines with depth, reflecting measurable structural variability.

657   Given the model's numerous constraints and limited degrees of freedom, the absolute energy is expected

658   to exceed that of reference groups. Cumulative mass weighting progressively stiffens the spline with

659   depth, allowing greater variability and thus higher energy near the surface while suppressing unrealistic

660   oscillations in deeper horizons, a limitation previously noted for equal-area splines below discrete

661   transitions (Odgers et al., 2012). The depth-resolved behavior reconstructed by phySpline aligns with

662   classical pedological concepts: horizon boundaries act as conceptual thresholds rather than abrupt

663   physical breaks (Schaetzl and Thompson, 2015). By preserving continuous gradients and minimising

664   rather than eliminating energy, phySpline retains information lost in purely geometric approaches (e.g.,

665   C-EAS) and accurately represents the vertical integration of pedogenic processes.

666   At the global scale, phySpline demonstrates strong generalization, as evidenced by the consistent overall

667   trend, decoupled uncertainties, and the energy-minimising regularisation term. These features indicate

668   that the method reliably captures soil structural patterns while preserving physically meaningful gradients

669   across diverse landscapes.

670   4.2.4   Provincial scale: spatial heterogeneity and profile coherence

671   Spatial analysis along with transect views of the phySplines were incorporated into the province scale

672   analysis. Spatial classification accuracy ranged from approximately 50 to 54% across depth intervals,

673   which was considered sufficient to support profile-level interpretation as it was consistent to other studies

674   (Chaney et al., 2016; Radočaj et al., 2023; Sabbaghi et al., 2024) for depth-function–based soil mapping

675   using national and continental scale maps (Bodenstein et al., 2022; Feeney et al., 2022; Simperegui et

676   al., 2025) with the high degree of vertical accuracy 96%.

677   The spatial prediction served primarily as a vehicle for assessing profile-scale behaviour across

678   contrasting landscapes (Figure 5) and the transects show the lateral view (Figure 6). The predicted maps

679   reflect various soil-forming processes across the province, ranging from aeolian deposits with deep S

680   enriched Psamments (Kandosols) and Calcids (Calcarasols) in the west supporting livestock. Deep C rich

681   Vertisols follow mafic/ultra-mafic parent material and the saline basins of the Murry-Darling Basin

682   network (Gray et al., 2016). Illuviation occurs with C accumulation around 30 to 60 cm on the stable

683   rolling hills of the western slopes in highly fertile Alfisols (Chromosols) supporting various crops (Scott

684   et al., 2007). The progression continues into the high-energy erosional regimes of the Eastern Highlands,

685   which are characterised by fluctuating soil states and types, and finally to the dynamic alluvial deposition

686   of the floodplains (Pain et al., 2011; Searle, 2021).

687   The transect visualisations are a great tool for environmental models with their essential movement from

688   the academic to the public domain where clear communication and visualisation are critical (Dahlstrom,

689   2014; Pandey et al., 2014; Vereecken et al., 2016). Smooth, laterally coherent depth transitions were

690   maintained across both transects despite strong contrasts in visualisation techniques, soil type and

691   landscape position. The transects reflect what was seen in the two-dimensional maps and help visualise

692   the more realistic multi-dimensional state of soil where three-dimensional soil mapping is becoming

693   more important (Lin et al., 2025). Therefore, with this knowledge and visualisation method, it becomes

694   viable not only to interpolate unseen classes but also to predict and visualise unseen profiles based on

695   soil types or geomorphic patterns using the framework from Wiese et al. (2016).

696   Despite pronounced class imbalance, dominant textures such as C remained stable and were

697   underpredicted by less than 1% (Table 7), while low-prevalence classes such as SiC, SiCL and SiL were

698   overpredicted by small margins of 0.67% or less. Misclassifications occurred systematically among

699   adjacent texture classes, reflecting transitional uncertainty rather than failure to capture dominant textures

700   and was not a result of class numbers. Class-resolved structural diagnostics corroborated these findings

701   (Figure 7). Integrated process scores remained low across all texture classes (0.20–0.77), with

702   contributions dominated by internal curvature rather than boundary mismatches or boundary

703   discontinuities. Transitional textures exhibited slightly higher internal energy, consistent with their

704   pedological role as intermediate textures rather than discrete endmembers. This indicates that the model

705   complexity is concentrated on resolving the fluid gradients between these textural poles rather than

706   correcting for mathematical inconsistencies at the horizon interfaces.

707   The province scale showed the visualisation power of classification and the predictions closely followed

708   the spatial patterns of NSW lithology maps (Gray et al., 2016) and Australian soil classification map

709   (Malone et al., 2025). While this correspondence is expected due to shared environmental covariates,

710   phySpline reproduces these patterns through a physics-informed framework, rather than explicit spatial

711   tuning. This suggests that spatial soil class predictions can be interpreted as expressions of underlying

712 potential energy gradients and self-regularisation of Euler's cumulative mass process, an implication that
713 warrants further investigation.

4.2.5 Local scale: linking spline behaviour to pedogenetic processes

715 At the local scale, the phySpline facilitated direct interpretation of soil-forming processes by integrating
716 depth-continuous predictions with environmental covariates. The Neno District dataset included 65 soil
717 profiles with well-represented soil texture classes, from which six profiles were selected for detailed
718 analysis across a range of slopes, elevations, precipitation regimes and landform elements (Figure 8;
719 Figure 2). Selected profiles varied in depth from 35 to 180 cm and encompassed shallow, coarse-textured
720 soil (LS-SL) to a deep, fine-textured soil (SC-C).

721 In many profiles, additional interpolated texture classes emerged (11 classes) relative to the original
722 observations (7 classes), reflecting the spline's ability to resolve transitional states that are typically
723 unobserved yet pedologically plausible. This highlights the complexity of categorical transitions often
724 overlooked by conventional models and demonstrates that these transitions can be captured
725 deterministically and analytically, without relying on fuzzy-set approaches. Most profiles exhibited
726 systematic enrichment in finer particles with depth, consistent with percolation-driven clay translocation
727 processes such as lessivage.

728 Different topography, precipitation, temperature and slope position all reflect the differences in the
729 profiles seen (Table 8). Nevertheless, it was thought that geology, vegetation and time were the main
730 environmental factors contributing to the pattern of soil patterns seen, factors that are more difficult to
731 examine due to timescales and dynamics. In the Neno mountain region, stabilising vegetation enhanced
732 water infiltration and reduced surface runoff, thus promoting clay accumulation in the upper subsoil,
733 consistent with previous findings on soil–vegetation interactions on mafic substrates (De Baets et al.,
734 2006; Gyssels et al., 2005).

735 Particularly in profiles C and F, these were interpretable in terms of lateral water movement and

736 landscape position rather than vertical drainage, both showing a pronounced clay increase around 10–15

737 cm. This reflects downslope translocation of clay influenced by steep slopes (>9%), where erosion has

738 depleted the topsoil, exposing the clay-rich subsoil. Profile E was found in a similar location but with a

739 slope of 16%, and it was inferred that erosion had completely removed the topsoil. Profiles A, B, and D

740 are located in the Lisungwe Valley on sloping positions with light textures (LS–SL), where water moves

741 predominantly vertically on spur, slope, and hollow positions. Profile D is deeper, most likely due to the

742 accumulation potential of hollows, as it is a concave slope, unlike a spur, which is a convex slope.

743 Profiles A, B and D overshot their endmember classes; however, this occurred in a mass-conservative

744 manner and resulted in representations that were more pedologically realistic than solutions constrained

745 to remain strictly within class bounds. Profiles C and F did not overshoot their endmembers and were

746 initially consistent with expected pedological structure. However, Profile F required the center of mass

747 to be shifted toward the top of the horizon to achieve a more realistic representation.

748 These observations are particularly important for depth harmonisation, as they demonstrate that

749 uncertainty patterns were largely decoupled from continuous interpolations. This indicates that the

750 imposed boundary constraints maintained numerical stability and continuity, while mitigating limitations

751 previously associated with drift effects. The partial independence between uncertainty estimates and

752 interpolated class assignments gives phySpline distinct practical and conceptual utility. Whereas high

753 uncertainty is often interpreted as misclassification or insufficient sample support, in phySpline

754 uncertainty is directly proportional to proximity to a class transition. In the Neno District, classifications

755 were largely correct, and elevated uncertainties consistently reflected transitional states rather than model

756 failure, indicating a measure that can be meaningfully used in practice without complexity.

4.2.6 Transferability, data requirements and limitations

The consistent performance of phySpline across global, provincial, and local scales demonstrates its robustness and transferability beyond the regions explicitly evaluated. Unlike purely data-driven classifiers, phySplines are governed by the information by self-regularisation and minimising the potential energy, making predictions independent of spatial support or sample size. Consequently, variations in observation density do not compromise structural integrity or class transitions. Comparable accuracy, class balance, and process-based diagnostics were observed in both sparsely sampled regions (e.g., NSW) and densely sampled regions (e.g., Neno), despite differences in sampling density, landscape heterogeneity, and soil moisture regimes.

At minimum, phySplines require vertically ordered soil horizon observations with defined depth intervals and categorical texture assignments. The method tolerates missing horizons through controlled extrapolation, but at least two observed horizons are required to anchor the latent process curve. Each profile is solved independently, so performance is driven by the number and quality of profiles rather than spatial sampling density. Where not all texture classes are observed, phySplines can be informed that additional classes are permissible, allowing transitional classes to emerge naturally along the latent curve. Where latent ordering is not apparent (e.g., numerical classification) can be arranged according to physically meaningful attributes, such as diagnostic horizon moisture, drainage class or Munsell color. Importantly, unlike over-constrained spline formulations (e.g., C-EAS), phySplines do not become over-constrained, meaning additional constraints can be applied without compromising the solution.

Performance may degrade when profiles are extremely shallow and abrupt horizons, lack reliable vertical ordering or include inconsistently defined texture classes across surveys. Limitations inherent to taxonomic classification may influence spline performance. In soil science, C, Si and S are commonly measured and combined to define texture classes. Except for C, neither S nor Si represent dominant

classes or display systematic depth-dependent transitions at any scale, reflecting their limited influence on profile structure. This may arise from the specific USDA diagnostic dimensions used (S = 0.05–2.0 mm; Si = 0.002–0.05 mm) or from the GlobalSoilMap standard depth intervals. Prior studies have similarly noted that conventional taxonomic systems may be unable to fully capture their functional roles (Duniway et al., 2013; Hartemink, 2015; Morrow, 2023; Vigués Jorba et al., 2025). Consequently, the depth intervals may have either highlighted this limitation, contributed to its manifestation in the dataset or the soil texture classification did.

Future improvements could incorporate probabilistic uncertainty via Bayesian or Monte Carlo methods. While current deterministic interpolations are easily interpretable and support endmember reconstruction, probabilistic approaches could enhance risk assessment or climate-change modeling. Although the algorithm is computationally efficient (~101,568 profiles in <9 min), large raster datasets will require further optimisation, such as parallelisation or implementation on platforms like Google Earth Engine, building on recent advances in grid-based (Flynn et al., 2024). The phySpline framework could be extended to a multinomial or multi-dimensional latent space, allowing it to capture complex inter-class transitions while remaining physics-informed and interpretable, though adoption depends on acceptance of this multidimensional perspective.

4.2.7 Implications for taxonomic information and pedometrics

In practice, phySplines transform what was once a computational and conceptual bottleneck into a fully continuous, analytically tractable framework. By resolving chronic profile boundary instabilities and complex categorical transitions found in traditional splines, they maintain pedological realism through a system that is mass-conservative, energy minimising, self-regularising and analytically solvable. Their ability to handle class imbalances and remain transferable across diverse sampling densities opens the way for next-generation soil profile modelling. Ultimately, phySplines demonstrate that the complex

803 transitions inherent to pedological philosophy hold untapped potential for soil thermodynamic

804 multifunctionality; by quantifying these gradients, the framework converts static taxonomic observations

805 into a dynamic, interpretable story of the vertical soil continuum. This provides researchers,

806 policymakers and environmental models with a framework to meaningfully visualise and understand soil

807 complexity.

808 PhySplines employ the exact analytic integral of the Euler cumulative resistance process, which

809 integrates stiffness continuously across the full horizon thickness. This shift eliminates the "midpoint

810 trap," ensuring that both boundary and interior behaviour are informed by the actual distribution of

811 mechanical and structural resistance. By capturing the continuous cumulative effect of depth-dependent

812 stiffness, the method preserves physically consistent curvature, maintains exact horizon continuity and

813 allows boundary conditions to emerge naturally. The result is a fully physics-informed, analytically

814 tractable spline that represents the horizon as a continuous process rather than a discrete approximation,

815 providing a realistic profile view that is not over-constrained.

816 Crucially, this framework bridges the gap between taxonomic nomenclature and physical laws:

817 categorical shifts are treated as high-fidelity indicators of pedogenetic change. Traditional, over-

818 constrained numerical splines are replaced with a physics-informed, flexible system that respects both

819 soil processes and mathematical rigour. This approach captures complex landscape trends within a

820 deterministic framework, mimicking the experience of traversing a terrain where environmental

821 gradients blend seamlessly into distinct soil classes. By resolving previously unmodelled transitions,

822 phySplines preserve taxonomic fidelity without sacrificing mathematical precision, offering a visually

823 accurate and interpretable way to "see" between horizons.

Conclusion

This study introduced phySpline, a physics informed, analytically solvable spline for interpolating categorical soil classes across depth. By embedding pedological philosophy including continuity whether gradual or virtually discrete and horizon boundary constraints into a fully continuous and differentiable framework, phySpline captures both observed and previously unmodeled transitional states, preserving process-based gradients that reflect real soil processes. Across global, provincial and local scales, phySpline achieved high classification accuracy while maintaining mass preservation, potential energy minimisation and pedological fidelity within a deterministic model. By bridging soil texture classes and exact integrals, phySpline maintains interpretability and supports effective communication within a mathematically robust framework. By resolving complex transitions and anchoring profile terminals, phySpline transforms discrete, human-assigned classes into continuous, physically meaningful representations. Future applications should extend this framework to multinomial and continuous properties, establishing a multifunctional platform that integrates physics-informed constraints with data-driven modeling to advance a new paradigm for profile-level soil interpolations and multi-disciplinary interpretations.

References

Amundson, R., Sanderman, J., Yoo, K., Chitsaz, M., Abramova, A., Georgiou, K., 2025. Neglecting vertical transport leads to underestimated soil carbon dynamics. Nat. Geosci. 18, 1239–1244. https://doi.org/10.1038/s41561-025-01846-6

Araya, Y.N., Emmott, A., Rawes, W., Zuza, E.J., 2023. Promoting climate-smart sustainable agroforestry to tackle social and environmental challenges: The case of macadamia agroforestry in Malawi. Journal of Agriculture and Food Research 14, 100846–100846. https://doi.org/10.1016/j.jafr.2023.100846

ASRIS, 2024. ASRIS - Australian Soil Resource Information System.

848   Australian Bureau Of Meteorology, 2019. Australian Gridded Climate Data (AGCD).

849   Basu, S., Isik, M.U., 2020. Categorical Complexity. Forum of Mathematics, Sigma.

850   https://doi.org/10.48550/ARXIV.1610.07737

851   Benbi, D.K., Toor, A.S., 2026. Spatial and Depth Distribution of Soil Carbon and Nitrogen in Relation

852   to Agricultural Management, Climate and Textural Control on Carbon Sequestration Potential.

853   Communications in Soil Science and Plant Analysis 57, 248–267.

854   https://doi.org/10.1080/00103624.2025.2589768

855   Bishop, T.F.A., McBratney, A.B., Laslett, G.M., 1999. Modeling soil attribute depth functions with equal-

856   area quadratic smoothing splines. Geoderma 91, 27–45. https://doi.org/10.1016/S0016-

857   7061(99)00003-8

858   Blewett, ichard (Ed.), 2012. Shaping a Nation: A Geology of Australia. ANU Press.

859   https://doi.org/10.22459/SN.08.2012

860   Bodenstein, D., Clarke, C., Watson, A., Miller, J., Van Der Westhuizen, S., Rozanov, A., 2022. Evaluation

861   of global and continental scale soil maps for southern Africa using selected soil properties.

862   CATENA 216, 106381. https://doi.org/10.1016/j.catena.2022.106381

863   Bortolus, A., 2008. Error Cascades in the Biological Sciences: The Unwanted Consequences of Using

864   Bad Taxonomy in Ecology. AMBIO: A Journal of the Human Environment 37, 114–118.

865   https://doi.org/10.1579/0044-7447(2008)37%255B114:ECITBS%255D2.0.CO;2

866   Buol, S.W., Southard, R.J., Graham, R.C., McDaniel, P.A., 2011. Soil Genesis and Classification, 1st ed.

867   Wiley. https://doi.org/10.1002/9780470960622

868   Burrough, P.A., Van Gaans, P.F.M., Hootsmans, R., 1997. Continuous classification in soil survey: Spatial

869   correlation, confusion and boundaries. Geoderma 77, 115–135. https://doi.org/10.1016/S0016-

870   7061(97)00018-9

871   Chaney, N.W., Wood, E.F., McBratney, A.B., Hempel, J.W., Nauman, T.W., Brungard, C.W., Odgers,

872   N.P., 2016. POLARIS: A 30-meter probabilistic soil series map of the contiguous United States.

873   Geoderma 274, 54–67. https://doi.org/10.1016/j.geoderma.2016.03.025

874   Cheng, C., Messerschmidt, L., Bravo, I., Waldbauer, M., Bhavikatti, R., Schenk, C., Grujic, V., Model,

875   T., Kubinec, R., Barceló, J., 2024. A General Primer for Data Harmonization. Sci Data 11, 152.

876   https://doi.org/10.1038/s41597-024-02956-3

877   Cohen, J., 1960. A Coefficient of Agreement for Nominal Scales. Educational and Psychological

878   Measurement 20, 37–46. https://doi.org/10.1177/001316446002000104

879   Colwell, J.D., 1970. A statistical-chemical characterization of four great soil groups in Southern New

880   South Wales based on orthogonal polynomials. Soil Research 8, 221–238.

881   CSIRO, 2024. Australian Soil Resource Information System Website. Data Collection.

882   Dahlstrom, M.F., 2014. Using narratives and storytelling to communicate science with nonexpert

883   audiences. Proc. Natl. Acad. Sci. U.S.A. 111, 13614–13620.

884   https://doi.org/10.1073/pnas.1320645111

885   De Baets, S., Poesen, J., Gyssels, G., Knapen, A., 2006. Effects of grass roots on the erodibility of topsoils

886   during concentrated flow. Geomorphology 76, 54–67.

887   https://doi.org/10.1016/j.geomorph.2005.10.002

888   Duniway, M.C., Miller, M.E., Brown, J., Toevs, G., 2013. An alternative to soil taxonomy for describing

889   key soil characteristics. Frontiers in Ecol & Environ 11, 527–528.

890   https://doi.org/10.1890/13.WB.020

891   Feeney, C.J., Cosby, B.J., Robinson, D.A., Thomas, A., Emmett, B.A., Henrys, P., 2022. Multiple soil

892   map comparison highlights challenges for predicting topsoil organic carbon concentration at

893   national scale. Sci Rep 12, 1379. https://doi.org/10.1038/s41598-022-05476-5

894   Fick, S.E., Hijmans, R.J., 2017. WorldClim 2: new 1km spatial resolution climate surface for global land

895   areas. International Journal of Climatology 37, 4302–4315.

896   Flynn, T., de Clercq, W., Rozanov, A., Clarke, C., 2019. High-resolution digital soil mapping of multiple

897   soil properties: an alternative to the traditional field survey? South African Journal of Plant and

898   Soil 1–11. https://doi.org/10.1080/02571862.2019.1570566

899   Flynn, T., Kostecki, R., Rebi, A., Raza, T., 2024. Accessing global soil raster images and equal-area

900   splines to estimate soil organic carbon stocks on the regional scale. Pedosphere

901   S1002016024000699. https://doi.org/10.1016/j.pedsph.2024.07.004

902   Flynn, T., Rozanov, A., Ellis, F., de Clercq, W., Clarke, C., 2022a. Farm-scale digital soil mapping of soil

903   classes in South Africa. South African Journal of Plant and Soil.

904   https://doi.org/10.1080/02571862.2022.2059115

905   Flynn, T., Wiese, L., Rozanov, A., 2022b. Soil carbon stock assessment using depth and spatial models

906   on afforested arable lands. South African Journal of Plant and Soil 1–13.

907   https://doi.org/10.1080/02571862.2022.2079741

908   Gray, J.M., Bishop, T.F.A., Wilford, J.R., 2016. Lithology and soil relationships for soil modelling and

909   mapping. CATENA 147, 429–440. https://doi.org/10.1016/j.catena.2016.07.045

910   Gyssels, G., Poesen, J., Bochet, E., Li, Y., 2005. Impact of plant roots on the resistance of soils to erosion

911   by water: a review. Progress in Physical Geography: Earth and Environment 29, 189–217.

912   https://doi.org/10.1191/0309133305pp443ra

913   Hartemink, A.E., 2015. The use of soil classification in journal papers between 1975 and 2014. Geoderma

914   Regional 5, 127–139. https://doi.org/10.1016/j.geodrs.2015.05.002

915   Hastie, T., Tibshirani, R., Friedman, J., 2009. The Elements of Statistical Learning, 2nd ed. Springer

916   Series in Statistics.

917   Henderson, M.M., Serences, J.T., Rungratsameetaweemana, N., 2025. Dynamic categorization rules alter

918   representations in human visual cortex. Nat Commun 16, 3459. https://doi.org/10.1038/s41467-

919   025-58707-4

920   Hillebrand, H., Blasius, B., Borer, E.T., Chase, J.M., Downing, J.A., Eriksson, B.K., Filstrup, C.T.,
921   Harpole, W.S., Hodapp, D., Larsen, S., Lewandowska, A.M., Seabloom, E.W., Van De Waal,
922   D.B., Ryabov, A.B., 2018. Biodiversity change is uncoupled from species richness trends:
923   Consequences for conservation and monitoring. Journal of Applied Ecology 55, 169–184.
924   https://doi.org/10.1111/1365-2664.12959

925   Hillel, D., 1998. Environmental Soil Physics, Journal of Environment Quality. Academic Press, San
926   Diego, CA. https://doi.org/10.2134/jeq1999.00472425002800060046x

927   Isaac, N., 2004. Taxonomic inflation: its influence on macroecology and conservation. Trends in Ecology
928   & Evolution 19, 464–469. https://doi.org/10.1016/j.tree.2004.06.004

929   ISRIC, 2021. World Soil Information Service (WoSIS). ISRIC - World Soil Information.

930   Jenny, H., 1941. Factors of Soil Formation: A System of Quantitative Pedology. McGraw- Hill, NY.
931   https://doi.org/10.2307/211491

932   Kempen, B., Brus, D.J., Stoorvogel, J.J., 2011. Three-dimensional mapping of soil organic matter content
933   using soil type-specific depth functions. Geoderma 162, 107–123.

934   Kienast-Brown, S., Philippe, J., Nauman, T., Libohova, Z., Roecker, S., Thompson, J., 2021. Comparison
935   of Spline Depth Interval and Point-Depth Approaches for Predicting Soil Properties. Presented at
936   the 2021 NCSS (National Cooperative Soil Survey) National Conference., USDA-NRCS.

937   Kleidon, A., 2010. Life, hierarchy, and the thermodynamic machinery of planet Earth. Physics of Life
938   Reviews 7, 424–460. https://doi.org/10.1016/j.plrev.2010.10.002

939   Kuhn, M., Johnson, K., 2013. Applied Predictive Modeling. Springer New York.
940   https://doi.org/10.1007/978-1-4614-6849-3

941   Leewis, M.-C., Lawrence, C.R., Schulz, M.S., Tfaily, M.M., Ayala-Ortiz, C.O., Flores, G.E.,
942   Mackelprang, R., McFarland, J.W., 2022. The influence of soil development on the depth
943   distribution and structure of soil microbial communities. Soil Biology and Biochemistry 174,
944   108808. https://doi.org/10.1016/j.soilbio.2022.108808

945   Lin, Z., Xu, J., Lu, M., 2025. Enhanced three-dimensional mapping of soil texture components using

946   quantile regression forest and spline techniques in Jiangsu Province, China. Sci Rep 16, 1646.

947   https://doi.org/10.1038/s41598-025-31144-5

948   Ma, Y., Condon, L.E., Koch, J., Bennett, A., Defnet, A., Tijerina-Kreuzer, D., Melchior, P., Maxwell,

949   R.M., 2026. High resolution US water table depth estimates reveal quantity of accessible

950   groundwater. Commun Earth Environ 7, 45. https://doi.org/10.1038/s43247-025-03094-3

951   Malone, B., Searle, R., 2022. Soil and Landscape Grid National Soil Attribute Maps - Sand (3"

952   resolution) - Release 2. https://doi.org/10.25919/RJMY-PA10

953   Malone, B.P., McBratney, A.B., Minasny, B., Laslett, G.M., 2009. Mapping continuous depth functions

954   of soil carbon storage and available water capacity. Geoderma 154, 138–152.

955   https://doi.org/10.1016/j.geoderma.2009.10.007

956   Malone, B.P., Searle, R., Stenson, M., McJannet, D., Zund, P., Román Dobarco, M., Wadoux, A.M.J.-C.,

957   Minasny, B., McBratney, A., Grundy, M., 2025. Update and expansion of the soil and landscape

958   grid of Australia. Geoderma 455, 117226. https://doi.org/10.1016/j.geoderma.2025.117226

959   McDougall, K.L., Hardy, G.E.S.J., Hobbs, R.J., 2002. Distribution of Phytophthora cinnamomi in the

960   northern jarrah (Eucalyptus marginata) forest of Western Australia in relation to dieback age and

961   topography. Australian Journal of Botany 50, 107–107. https://doi.org/10.1071/BT01040

962   Morrow, K.H., 2023. A Scale Problem with the Ecosystem Services Argument for Protecting

963   Biodiversity. Environmental Values 32, 271–290.

964   https://doi.org/10.3197/096327122X16569260361751

965   NSW Department of Primary Industries, 2020. Agricultural production in New South Wales: Crop

966   statistics. NSW Government.

967   Odgers, N.P., Libohova, Z., Thompson, J.A., 2012. Equal-area spline functions applied to a legacy soil

968   database to create weighted-means maps of soil organic carbon at a continental scale. Geoderma

969   189–190, 153–163. https://doi.org/10.1016/j.geoderma.2012.05.026

970   Odom, W., Doctor, D., 2023. Rapid estimation of minimum depth-to-bedrock from lidar leveraging deep-

971   learning-derived surficial material maps. Applied Computing and Geosciences 18, 100116.

972   https://doi.org/10.1016/j.acags.2023.100116

973   Pain, C., Gregory, L., Wilson, P., McKenzie, N., 2011. Physiographic Regions of Australia.

974   https://doi.org/10.25919/52XM-CH28

975   Pandey, A.V., Manivannan, A., Nov, O., Satterthwaite, M., Bertini, E., 2014. The Persuasive Power of

976   Data Visualization. IEEE Trans. Visual. Comput. Graphics 20, 2211–2220.

977   https://doi.org/10.1109/TVCG.2014.2346419

978   Pei, J., Li, J., Luo, Y., Rillig, M.C., Smith, P., Gao, W., Li, B., Fang, C., Nie, M., 2025. Patterns and

979   drivers of soil microbial carbon use efficiency across soil depths in forest ecosystems. Nat

980   Commun 16, 5218. https://doi.org/10.1038/s41467-025-60594-8

981   Ponce-Hernandez, R., Marriott, F.H.C., Beckett, P.H.T., 1986. An improved method for reconstructing a

982   soil profile from analyses of a small number of samples. Journal of Soil Science 37, 455–467.

983   Probst, A.J., Ladd, B., Jarett, J.K., Geller-McGrath, D.E., Sieber, C.M.K., Emerson, J.B., Anantharaman,

984   K., Thomas, B.C., Malmstrom, R.R., Stieglmeier, M., Klingl, A., Woyke, T., Ryan, M.C.,

985   Banfield, J.F., 2018. Differential depth distribution of microbial function and putative symbionts

986   through sediment-hosted aquifers in the deep terrestrial subsurface. Nat Microbiol 3, 328–336.

987   https://doi.org/10.1038/s41564-017-0098-y

988   Radočaj, D., Jurišić, M., Rapčan, I., Domazetović, F., Milošević, R., Plaščak, I., 2023. An Independent

989   Validation of SoilGrids Accuracy for Soil Texture Components in Croatia. Land 12, 1034.

990   https://doi.org/10.3390/land12051034

991   Rogozovsky, I., Ansmann, A., Hofer, J., Chudnovsky, A., 2025. Unveiling Atmospheric Layers: Vertical

992   Pollution Patterns and Prospects for High-Resolution Aerosol Retrievals Using the Eastern

993   Mediterranean as a Case Study. Environ. Sci. Technol. 59, 12181–12195.

994   https://doi.org/10.1021/acs.est.4c14556

995   Ruiz, O.E., Wagenaar, J.B., Mehta, B., Ziogas, I., Swanson, L., Worley, K.C., Cruz-Almeida, Y., Johnson,

996   A.J., Boline, J., Boccanfuso, J., Martone, M.E., Haelterman, N.A., 2025. A guide to developing

997   harmonized research workflows in a team science context. Experimental Neurology 392, 115333.

998   https://doi.org/10.1016/j.expneurol.2025.115333

999   Russell, J.S., Moore, A.W., 1968. Comparison of different depth weighting in the numerical analysis of

1000   anisotropic soil profile data. Presented at the Transaction of the 9th International Congress,

1001   International Soil Science Society, Adelaide, Australia, pp. 205–213.

1002 Sabbaghi, M.A., Esfandiari, M., Eftekhari, K., Torkashvand, A.M., 2024. Predictive map of soil texture

1003   classes using decision tree model and neural network with features of geomorphology level. Can.

1004   J. Soil. Sci. 104, 72–90. https://doi.org/10.1139/cjss-2023-0011

1005 Schaetzl, R.J., Thompson, M.L., 2015. Soils: genesis and geomorphology, Second edition. ed. Cambridge

1006   University Press, New York, NY.

1007 Scott, B.J., Fenton, I.G., Fanning, A.G., Schumann, W.G., Castleman, L.J.C., 2007. Surface soil acidity

1008   and fertility in the eastern Riverina and Western Slopes of southern New South Wales. Aust. J.

1009   Exp. Agric. 47, 949. https://doi.org/10.1071/EA05155x

1010 Searle, R., 2021. Soil and Landscape Grid National Soil Attribute Maps - Australian Soil Classification

1011   Map (3" resolution) - Release 1. https://doi.org/10.25919/VKJN-3013

1012 Simperegui, K.B.D., Kouame, A.K.K., Kwesie, B., Bindraban, P.S., Adzawla, W., Asamoah, E., El

1013   Gharous, M., 2025. Digital mapping of Ghana's soil properties and nutrients: performance of

1014   spline   and   weighted   average   approaches.   Geoderma   459.

1015   https://doi.org/10.1016/j.geoderma.2025.117365

1016 Smith, J.A., Robert B. Thompson, 2019. Livestock Production in New South Wales: Current Trends and

1017   Future Projections. Australian Journal of Agricultural Science 54, 125–140.

1018 Souza, L.F.T., Hirmas, D.R., Sullivan, P.L., Reuman, D.C., Kirk, M.F., Li, L., Ajami, H., Wen, H., Sarto,

1019   M.V.M., Loecke, T.D., Rudick, A.K., Rice, C.W., Billings, S.A., 2023. Root distributions,

precipitation, and soil structure converge to govern soil organic carbon depth distributions. Geoderma 437, 116569. https://doi.org/10.1016/j.geoderma.2023.116569

Vereecken, H., Schnepf, A., Hopmans, J.W., Javaux, M., Or, D., Roose, T., Vanderborght, J., Young, M.H., Amelung, W., Aitkenhead, M., Allison, S.D., Assouline, S., Baveye, P., Berli, M., Brüggemann, N., Finke, P., Flury, M., Gaiser, T., Govers, G., Ghezzehei, T., Hallett, P., Hendricks Franssen, H.J., Heppell, J., Horn, R., Huisman, J.A., Jacques, D., Jonard, F., Kollet, S., Lafolie, F., Lamorski, K., Leitner, D., McBratney, A., Minasny, B., Montzka, C., Nowak, W., Pachepsky, Y., Padarian, J., Romano, N., Roth, K., Rothfuss, Y., Rowe, E.C., Schwen, A., Šimůnek, J., Tiktak, A., Van Dam, J., Van Der Zee, S.E.A.T.M., Vogel, H.J., Vrugt, J.A., Wöhling, T., Young, I.M., 2016. Modeling Soil Processes: Review, Key Challenges, and New Perspectives. Vadose Zone Journal 15, 1–57. https://doi.org/10.2136/vzj2015.09.0131

Vigués Jorba, J., Scherrer, D., Duchenne, F., Zellweger, F., Gossner, M.M., Bollmann, K., 2025. Differential responses of taxonomic, functional and phylogenetic multi-taxa diversity to environmental factors in temperate forest ecosystems. Ecological Indicators 178, 113855. https://doi.org/10.1016/j.ecolind.2025.113855

Viscarra Rossel, R., Chen, C., Grundy, M., Searle, R., Clifford, D., Odgers, N., Holmes, K., Griffin, T., Liddicoat, C., Kidd, D., 2014. Soil and Landscape Grid National Soil Attribute Maps - Soil Depth (3" resolution) - Release 1. https://doi.org/10.4225/08/546F540FE10AA

Weiskopf, S.R., Myers, B.J.E., Arce-Plata, M.I., Blanchard, J.L., Ferrier, S., Fulton, E.A., Harfoot, M., Isbell, F., Johnson, J.A., Mori, A.S., Weng, E., HarmáCˇková, Z.V., Londoño-Murcia, M.C., Miller, B.W., Pereira, L.M., Rosa, I.M.D., 2022. A Conceptual Framework to Integrate Biodiversity, Ecosystem Function, and Ecosystem Service Models. BioScience 72, 1062–1073. https://doi.org/10.1093/biosci/biac074

1043   Wiese, L., Ros, I., Rozanov, A., Boshoff, A., de Clercq, W., Seifert, T., 2016. An approach to soil carbon

1044   accounting and mapping using vertical distribution functions for known soil types. Geoderma

1045   263, 264–273. https://doi.org/10.1016/j.geoderma.2015.07.012

1046   Yanofsky, N.S., 2015. Computability and Complexity of Categorical Structures.

1047   https://doi.org/10.48550/ARXIV.1507.05305

1048   Zhang, J., Goodchild, M.F., 2002. Uncertainty in Geographical Information, 0 ed. CRC Press.

1049   https://doi.org/10.1201/b12624

1050   Zhang, X., Zhang, W.-C., Wu, W., Liu, H.-B., 2023. Horizontal and vertical variation of soil clay content

1051   and its controlling factors in China. Science of The Total Environment 864, 161141.

1052   https://doi.org/10.1016/j.scitotenv.2022.161141

1053   Zhao, S., Kvale, K.F., Zhu, L., Zettler, E.R., Egger, M., Mincer, T.J., Amaral-Zettler, L.A., Lebreton, L.,

1054   Niemann, H., Nakajima, R., Thiel, M., Bos, R.P., Galgani, L., Stubbins, A., 2025. The distribution

1055   of subsurface microplastics in the ocean. Nature 641, 51–61. https://doi.org/10.1038/s41586-025-

1056   08818-1

1057